A CATALOG OF 203 GALAXY CLUSTERS SERENDIPITOUSLY DETECTED IN THE ROSAT PSPC POINTED OBSERVATIONS[1]

A. VIKHLININ,[2] B. R. MCNAMARA, W. FORMAN, AND C. JONES

Harvard-Smithsonian Center for Astrophysics, 60 Garden Street, Cambridge, MA 02138; avikhlinin@cfa.harvard.edu, bmcnamara@cfa.harvard.edu, wforman@cfa.harvard.edu, cjones@cfa.harvard.edu

H. QUINTANA[3]

Departamento de Astronomia y Astrofisica, Pontificia Universidad Catolica, Casilla 104, 22 Santiago, Chile

AND

A. HORNSTRUP

Danish Space Research Institute, Juliane Maries Vej 30, 2100 Copenhagen O, Denmark

Received 1998 January 12; accepted 1998 March 6

ABSTRACT

We present a catalog of 203 clusters of galaxies serendipitously detected in 647 ROSAT PSPC high Galactic latitude pointings covering 158 deg^2. This is one of the largest X-ray–selected cluster samples, comparable in size only to the ROSAT All-Sky Survey sample of nearby clusters (Ebeling et al. 1997). We detect clusters in the inner 17′.5 of the ROSAT PSPC field of view using the spatial extent of their X-ray emission. Fluxes of detected clusters range from 1.6×10^{-14} to 8×10^{-12} ergs s^{-1} cm^{-2} in the 0.5–2 keV energy band. X-ray luminosities range from 10^{42} ergs s^{-1}, corresponding to very poor groups, to $\sim 5 \times 10^{44}$ ergs s^{-1}, corresponding to rich clusters. The cluster redshifts range from $z = 0.015$ to $z > 0.5$. The catalog lists X-ray fluxes, core radii, and spectroscopic redshifts for 73 clusters and photometric redshifts for the remainder. Our detection method, optimized for finding extended sources in the presence of source confusion, is described in detail. Selection effects necessary for a statistical analysis of the cluster sample are comprehensively studied by Monte Carlo simulations. We have optically confirmed 203 of 223 X-ray sources as clusters of galaxies. Of the remaining 20 sources, 19 are likely false detections arising from blends of unresolved point X-ray sources. Optical identifications of the remaining object are hampered by a bright nearby star. Above a flux of 2×10^{-13} ergs s^{-1} cm^{-2}, 98% of extended X-ray sources are optically confirmed clusters. The number of false detections and their flux distribution are in perfect agreement with simulations. The log N–log S relation for clusters derived from our catalog shows excellent agreement with counts of bright clusters derived from the *Einstein* Extended Medium Sensitivity Survey and ROSAT All-Sky Survey. At fainter fluxes, our log N–log S relation agrees with the smaller area WARPS survey. Our cluster counts appear to be systematically higher than those from a 50 deg^2 survey by Rosati et al. In particular, at a flux of 2×10^{-13} ergs s^{-1} cm^{-2}, we find a surface density of clusters of 0.57 ± 0.07 deg^{-2}, which is a factor of 1.3 more than was found by Rosati et al. This difference is marginally significant at the $\sim 2\ \sigma$ level. The large area of our survey makes it possible to study the evolution of the X-ray luminosity function in the high luminosity range inaccessible with other, smaller area ROSAT surveys.

Subject headings: catalogs — galaxies: clusters: general — surveys — X-rays: galaxies

1. INTRODUCTION

Clusters of galaxies are among the most important objects for cosmological studies. Models of large-scale structure formation such as cold dark matter (CDM) predict that the abundance of clusters is determined by the spectrum of primordial perturbations and cosmological parameters Ω and Λ. Observations of clusters at different redshifts can be used to constrain these parameters (see, e.g., White & Rees 1978; Kaiser 1986; White, Efstathiou, & Frenk 1993; Henry & Arnaud 1991; Viana & Liddle 1996; Henry 1997). Following a different approach, observations of the Sunyaev-Zeldovich effect (Sunyaev & Zeldovich 1972) in a large sample of distant clusters can be used for a direct measurement of the distance to these clusters, and can thus provide values of H_0 (see, e.g., Birkinshaw, Hughes, & Arnaud 1991) and q_0.

Up until the present, the largest samples of distant clusters resulted from optical surveys that searched for enhancements in the surface density of galaxies (see, e.g., Postman et al. 1996). This method suffers seriously from projection effects (see, e.g., van Haarlem, Frenk, & White 1997). Distant clusters found by such techniques as galaxy concentrations around distant radio sources (Dickinson 1996) or " dark " lenses (Hattori et al. 1997) cannot be considered as statistical samples. Of all methods for detecting distant clusters, X-ray surveys are the least sensitive to projection because the X-ray emission is proportional to the square of the density of the hot gas, which must be compressed in a deep potential well for us to detect it. It is noteworthy that, unlike optical surveys, X-ray surveys have the possibility of finding interesting objects such as " fossil " clusters in which almost all galaxies have merged to form a cD galaxy (Ponman et al. 1994), and hypothetical " failed " clusters in which galaxy formation was suppressed (Tucker, Tanan-

baum, & Remillard 1995). To date, the largest published sample of distant X-ray selected clusters is that from the *Einstein* Extended Medium Sensitivity Survey (EMSS; Goia et al. 1990; Stocke et al. 1991). However, because of its relatively high flux limit, the EMSS sample contains only 6 clusters at $z > 0.5$.

Finding clusters in X-rays is complicated by their rarity among other types of sources. A comparison of the log N–log S relations for all sources (Hasinger et al. 1993b) and clusters (this work) shows that at a flux of 10^{-14} ergs s^{-1} cm^{-2} in the 0.5–2 keV band, clusters comprise not more than 10%–20% of the total source population. The large amount of optical identification work needed for cluster selection can be greatly reduced if they are searched for among spatially extended X-ray sources. Even at $z = 1$, a rich cluster with a core radius of 250 kpc has an angular radius of $> 20''$, which still can be resolved with the *ROSAT* PSPC on-axis. Detection of extended sources requires new data analysis techniques. Even if the spatial extent is not used for cluster selection, special detection techniques are needed because clusters at $z \approx 0.2$–0.3 are 3–4 times broader than the *ROSAT* PSPC point-spread function.

The idea of selecting distant cluster samples from various *ROSAT* surveys was pursued by different groups in the past few years. Rosati et al. (1995, 1998) searched for clusters in long-exposure (>15 ks) *ROSAT* PSPC pointed observations with a total area of 50 deg^2, using optical identifications of all extended X-ray sources found by wavelet transform analysis. Their sample consists at present of 70 clusters. The Wide Angle *ROSAT* Pointed Survey (WARPS; Scharf et al. 1997; Jones et al. 1998) uses the Voronoi tessellation and percolation technique to detect both pointlike and extended sources, followed by optical identifications of all sources. The WARPS cluster sample consists at present of 46 clusters found in *ROSAT* pointings with exposures >8 ks, covering 16.2 deg^2. A small sample of 15 clusters at $0.3 < z < 0.7$ was identified by the SHARC survey (Collins et al. 1997). The RIXOS cluster sample (Castander et al. 1995) consists of 13 clusters, detected using a technique that was optimized for point sources. Their results on cluster evolution appear to contradict other *ROSAT* surveys (Collins et al. 1997), probably because the point-source detection algorithm had a low efficiency for detecting extended cluster emission. Finally, important information about the surface density of clusters at very low fluxes is provided by several very deep *ROSAT* pointings in which complete optical identifications are performed (see, e.g., McHardy et al. 1998). Note that because of the small area, none of the aforementioned surveys is able to study the luminosity function of distant clusters above 3×10^{44} ergs s^{-1}, where the deficit of high-redshift EMSS clusters was reported (Henry et al. 1992).

In this paper, we present a sample of distant clusters selected from 647 *ROSAT* PSPC observations of high Galactic latitude targets, covering a solid angle of 158 deg^2, a factor of 3 larger than the largest of the other *ROSAT* surveys. The source catalog includes 203 optically confirmed clusters and thus is one of the largest X-ray selected samples, comparable in size only to the *ROSAT* All-Sky Survey sample of nearby clusters (Ebeling et al. 1997). We detect cluster candidates as extended X-ray sources using the wavelet decomposition technique described in this paper and maximum-likelihood fitting to the surface brightness distributions to determine the significance of the source

extent. We then identify only significantly extended sources with optical follow-up observations. Optical observations confirm that 91% of our sources are indeed clusters of galaxies. Various selection effects, such as the fraction of clusters that remains unresolved or undetected, are studied using extensive Monte Carlo simulations. Comparison of the log N–log S relation for clusters derived from our and other *ROSAT* surveys shows that our cluster counts at the bright end are in excellent agreement with those from the *ROSAT* All-Sky Survey sample of Ebeling et al. (1997). At a flux of 2×10^{-13} ergs s^{-1} cm^{-2}, our log N–log S relation agrees well with the WARPS survey (Jones et al. 1998) but is somewhat higher than that found by Rosati et al. (1998).

Cluster size and flux estimates throughout the paper use $H_0 = 50$ km s^{-1} Mpc^{-1} and $q_0 = 0.5$. All X-ray fluxes and luminosities are reported in the 0.5–2 keV energy band.

2. X-RAY DATA

We analyzed only *ROSAT* PSPC pointings at high Galactic latitudes, $|b| > 30°$, and low absorption, $N_H < 6 \times 10^{20}$ cm^{-2}, excluding the 10° radius regions around the LMC and SMC. Low Galactic latitude fields were not used because the absorption is large and nonuniform in these regions, and because a high density of stars complicates optical identifications. We also excluded observations of extended targets, such as known clusters of galaxies, nearby galaxies, supernova remnants (SNRs), and star clusters. As the only exception, we included the $2146+0413$ pointing (*ROSAT* sequences 800150 and 800150a01), which was an X-ray follow-up of clusters selected optically in a blank field.

All individual *ROSAT* sequences with listed exposures longer than 2 ks, meeting the above criteria and publicly available by 1996 April, were extracted from the data archive at the Goddard Space Flight Center. Using S. Snowden's software, we cleaned the data excluding high background intervals. We also generated exposure maps using R4–R7 detector maps (energy range 0.5–2 keV) weighted according to the average PSPC background spectrum. Multiple observations of the same target were merged. Observations with cleaned exposures <1.5 ks were discarded. The final data set consists of 647 fields, schematically shown in Galactic coordinates in Figure 1. We used only hard-band images, 0.6–2 keV, which increases the sensitivity of cluster detection given that the spectrum of the *ROSAT* background is much softer than that of a typical cluster. This energy band is slightly different from that used for the exposure map generation, but this discrepancy
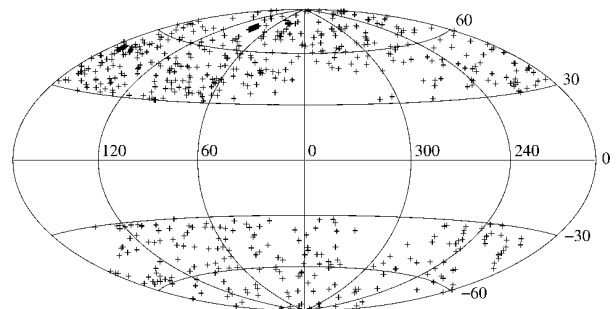

FIG. 1.—Distribution of *ROSAT* pointings in Galactic coordinates. The higher density in the Northern hemisphere is caused by a preferential choice of Northern objects as *ROSAT* targets.

results only in a very small, $<2\%$, error in the vignetting correction in the inner region of the field of view where clusters are detected. To oversample the point-spread function (PSF) adequately, an image-pixel size of $5''$ was chosen.

Our next step was to calculate the background map for each observation. The *ROSAT* PSPC background cannot be modeled simply using the exposure map template because of the nonuniformity of the cosmic X-ray background, the presence of scattered solar X-rays, and the wings of the PSF around bright sources. The angular correlation function of the XRB (Vikhlinin & Forman 1995; Soltan et al. 1996) predicts $\approx 10\%$ brightness fluctuations on a $10'$ scale. If not modeled, such background variations can cause errors in measured cluster fluxes. Since the best approximation to the background in each field is a smoothed source-subtracted image, we created background maps as follows. We first divided an image by its exposure map to remove the imprint of the PSPC window support structure. Using the wavelet decomposition technique (§ 3.2), we subtracted all sources with characteristic sizes $\leq 3'$ in radius and smoothed the cleaned image with a $\sigma = 6'$ Gaussian filter. The background map was finally obtained as a product of the smoothed image and the exposure map.

3. DETECTION OF EXTENDED SOURCES

3.1. *General Considerations*

Finding clusters in *ROSAT* PSPC images requires detection of sources of widely different angular size ranging from approximately the FWHM of the PSF, $\sim 25''$, to several arcminutes. Any algorithm for finding spatially extended sources solves two tasks: (1) source detection, i.e., identifying regions where the surface brightness significantly exceeds that of the background, and (2) determining extent, i.e., deciding whether the detected source is significantly broader than the point-spread function. The two-stage nature of extended source detection is not usually emphasized but can be seen in practice. Rosati et al. (1995) convolved images with wavelet kernels of varying scale to find sources and then derived the source extent from wavelet amplitudes. Scharf et al. (1997) used Voronoi tessellation and percolation (VTP) to find regions with enhanced surface brightness and then derived the source extent from the measured area and flux. Each of these methods has advantages for certain tasks. For example, VTP can find extended sources regardless of their shape. However, none of these methods is optimal for both parts of the problem. Obviously, the best sensitivity can be achieved if, at each stage, one uses a separate algorithm optimized for its task. We show below that our method of detecting sources using wavelets and determining source extent by maximum-likelihood fitting is theoretically close to optimum for finding regularly shaped clusters.

The optimal method of source detection is matched filtering (see, e.g., Pratt 1978). For faint sources, the filter is close in shape to the sources themselves, and any filter with a shape close to the matched one performs almost equally well (Press et al. 1992). Our wavelet detection method uses filters that approximate Gaussian distributions with $\sigma = 1$, $2, 4, \ldots$, pixels. Since these filters span a range of sizes, nearly optimal detection is achieved for circular sources of any size. With an axially symmetric filter, it is possible to miss very irregular sources. However, most clusters are rela-

tively regular (Jones & Forman 1998) for detection purposes. Also, this shortcoming is clearly outweighed by the merits of the wavelet method, such as optimal detection of sources with regular shape, complete background subtraction, and elimination of the influence of point sources. We discuss these issues below in detail.

Consider now the optimal method to discriminate between extended and point sources. Cluster radial surface brightness profiles can be described by the so-called β-model, $I(r, r_c) = I_0(1 + r^2/r_c^2)^{-3\beta + 0.5}$ (Cavaliere & Fusco-Femiano 1976). Therefore, to discriminate between a cluster and a point source, we should determine whether $I(r, r_c)$ with core radius $r_c > 0$ describes the data better than a δ-function, that is, $I(r, r_c)$ with $r_c = 0$. According to the *Neyman-Pearson Lemma* (see, e.g., Martin 1971), the most sensitive test for this problem is the change in the value of the likelihood function between the best-fit value of r_c and $r_c = 0$. Maximum-likelihood fitting may not be the best method for finding clusters with arbitrary shapes, but theoretically it is the best one for the vast majority of clusters having regular shapes.

Based on the considerations above, we implemented an algorithm for detection of extended sources that uses our own variant of wavelet transform analysis, wavelet decomposition, to find all sources even in the presence of source confusion and uses maximum-likelihood fitting of β-models to determine whether each source is extended. Each step is discussed below in detail.

3.2. *Wavelet Detection of Cluster Candidates*

Cluster detection in the *ROSAT* PSPC images is complicated by the varying background and confusion with point sources located in the vicinity of clusters. The wavelet transform is well suited to overcome these difficulties. We briefly outline the relevant properties of the wavelet transform and then describe our particular implementation.

3.2.1. *General Properties of the Wavelet Transform*

The basic idea of the wavelet transform applied to astronomical images (see, e.g., Grebenev et al. 1995, and references therein) is a convolution with a kernel that consists of a positive core and an outer negative ring, so that the integral of the kernel over the x, y plane is zero. The convolution with such kernels allows complete background subtraction and isolation of structures of particular angular size. This can be shown using a kernel that is the difference of two Gaussian components,

$$W(r) = \frac{\exp{(-r^2/2a^2)}}{2\pi a^2} - \frac{\exp{(-r^2/2b^2)}}{2\pi b^2}, \qquad (1)$$

where $b = 2a$. The convolution of this kernel with any linear function $s(x, y) = ax + by + c$ is zero. Therefore, any slowly varying background that can be locally approximated by a linear function is subtracted by a convolution with this kernel. To demonstrate the ability of wavelets to reveal structures with a given size, consider the convolution of the wavelet kernel with a Gaussian $\exp{(-r^2/2\sigma^2)}$. The convolution amplitude achieves its maximum when $\sigma = a\sqrt{2}$ but rapidly falls to $\frac{1}{2}$ of the maximum for $\sigma = a/2$ and $\sigma = 4a$. These properties of the wavelet transform are used for source detection (see, e.g., Damiani et al. 1997). In most applications, an image is convolved with a family of kernels of the same functional form while varying its scale (a in eq. [1]). Sources are detected as significant

local maxima in the convolved images. Information about the source angular extent can be derived from the wavelet transform values at different scales. This simple approach works well for detection of isolated sources but fails if another bright source is located nearby, as is shown in Figures 2a and 2b. A point source with a flux 4 times that of the cluster is located at $\frac{2}{3}$ core radii from the cluster center (a). The image is convolved with the wavelet kernels (eq. [1]) of scale $a = 1, 2, 4, \ldots, 32$ pixels (b). At each scale, the point source dominates the convolution, and the cluster remains undetected. A different kind of complication for a simple wavelet analysis is caused by compact groups of point sources. Convolved with a wide kernel, such groups appear as a single extended source, resulting in false cluster detections. Neither of these problems can be overcome by using a different symmetric wavelet kernel with compact support (Strag & Nguyen 1995). However, they can be overcome using the idea employed in the CLEAN algorithm commonly applied in radio astronomy (Högbom 1974): point sources are detected first and subtracted from the image before the detection of extended sources. Below, we describe our algorithm, which we call wavelet decomposi-
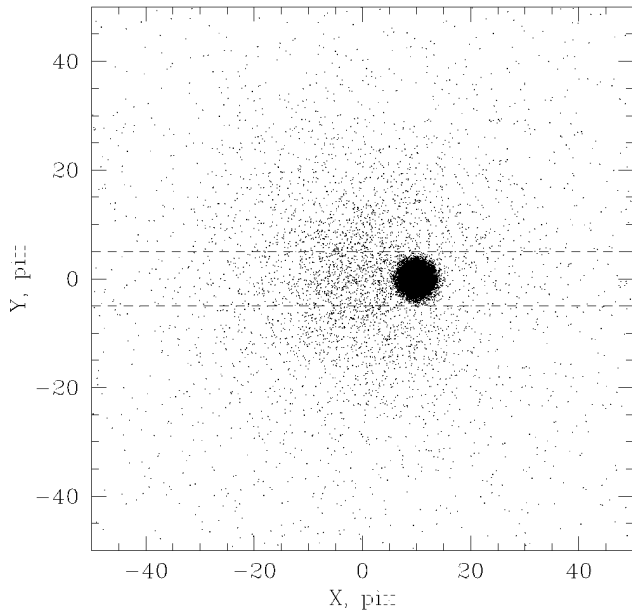
FIG. 2a
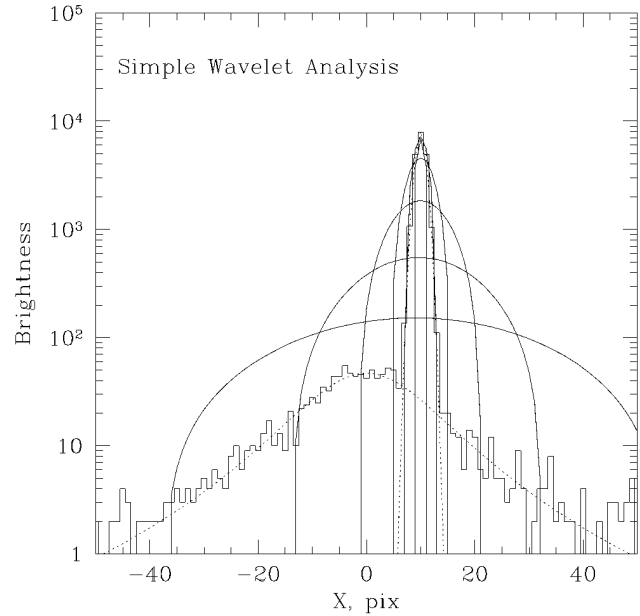
FIG. 2b
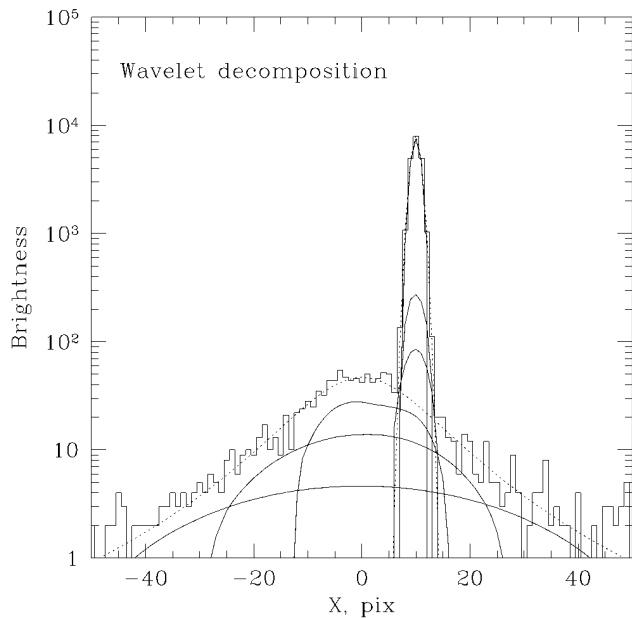
FIG. 2c
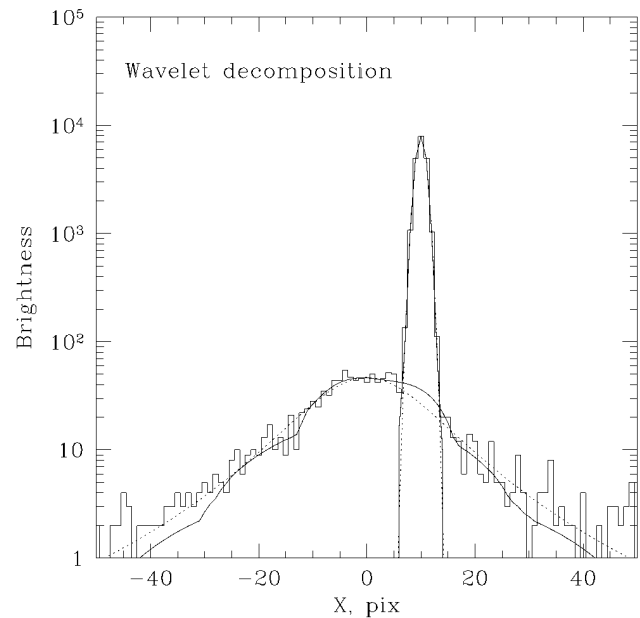
FIG. 2d

FIG. 2.—Advantage of the wavelet decomposition algorithm. (a) Bright point source is located in the vicinity of a cluster. Dashed lines show the strip in which brightness profiles (b)–(d) were extracted. (b) Result of convolution of this image with wavelet kernels (eq. [1]) with the scale $a = 1, 2, 4, \ldots, 32$ pixels. The data profile is shown by the solid histogram, and the profiles of convolved images by solid lines. At all scales, the convolution is dominated by the point source and there is no separate peak corresponding to the cluster. Therefore, the cluster remains undetected by this simple analysis. Our method (c) provides a decomposition of the original image into components with the characteristic size 1, 2, 4, ..., 32 pixels. Small-scale components model the point source. The cluster becomes apparent and well separated from the point source at large scales. The sum of the three smallest and three largest scales of the wavelet decomposition provide almost perfect decomposition of the raw image into its original components (d).

tion, which combines this approach with wavelet transform analysis.

3.2.2. Wavelet Decomposition

The family of wavelet kernels we use is given by equation (1), in which we use several combinations of a and b that we call scales. At scale 1, the positive component in equation (1) is a δ-function ($a = 0$) and $b = 1$ pixel. At scale 2, $a = 1$ and $b = 2$ pixels; at scale 3, $a = 2$ and $b = 4$ pixels; and so on. At the largest scale n, the kernel is a single, positive Gaussian component with $a = 2^{n-1}$ pixels. How close is this family of kernels to the optimal filter for detecting sources with the β-model surface brightness profiles? Numerical calculations show that in at least one of the scales, the signal-to-noise ratio exceeds 80% of the maximum value corresponding to the optimal filter—the β-model itself—for $0.55 < \beta < 0.8$.

The described family of wavelet kernels has the advantage of an easy and linear back transformation. The original image $z(x, y)$ is given by

$$z(x, y) = \sum_{j=1}^{n} w_j(x, y) , \qquad (2)$$

where $w_j(x, y)$ is the convolution with the kernel of scale j. An important interpretation of this wavelet transform follows from this equation: it provides a decomposition of an image into a sum of components of different characteristic sizes. With this interpretation, we construct the following iterative scheme to remove the effect of point sources.

We convolved the image with a kernel of the smallest scale, estimated the detection threshold as described below, and cleaned the image of noise. The convolved image values were preserved in those regions where the brightness exceeded $\frac{1}{2}$ of the detection threshold and that contained at least one maximum above the detection threshold. The remaining image was set to zero. We subtracted this cleaned image from the input image to remove the sources that have been detected at this step and repeated the convolution and cleaning procedure iteratively until no more sources were detected at this scale. We also added cleaned images obtained at each iteration to produce a composite image of significant sources detected at this scale. We then moved to the next scale, at which the input image was set to the original image minus everything detected at the first scale. The iterations were stopped at scale 6, for which $a = 80''$ and $b = 160''$ and detected sources have typical full widths of $3'-4'$.

The bottom panels of Figure 2 illustrate this procedure. The smallest wavelet kernel is insensitive to the broad cluster emission and detects only the point source. When iterations at scale 1 are completed, $\sim 90\%$ of the point source flux has been subtracted. Subtraction of the point source continues at scales 2 and 3, while the cluster remains undetected because it is broader than the analyzing kernel. The point source is almost completely subtracted at small scales and does not interfere with cluster detection at scales 4–6. The result of these iterations is a set of images containing statistically significant structures detected at each scale, whose characteristic size corresponds to the width of the analyzing kernel at this scale. Therefore, to separate point and extended sources, one can combine small and large scales, respectively. As Figure 2d shows, the sums of scales 1–3 and 4–6 provide almost perfect separation of the original image into the point source and the cluster.

It is important to choose the correct detection thresholds. Although several analytic methods of deriving detection thresholds for the wavelet transform were suggested (Starck & Pierre 1998, and references therein), we determined them through Monte Carlo simulations. We simulated 512×512 images consisting of a flat Poisson background and convolved them with the wavelet kernels. The distribution of the local maxima in the convolved images was used to define the detection threshold. We set this threshold at that value above which one expects to find on average $\frac{1}{3}$ local maxima per simulated background image per scale in the absence of real sources, so that in the combined scales 4–6 we expect one false detection per image. Thus defined, detection thresholds correspond to a formal significance of $\approx 4.5 \, \sigma$. Detection thresholds were tabulated for a grid of simulated background intensities. In the analysis of real images, we estimated the local background and found the detection threshold by interpolation over the precalculated grid. Detection thresholds were deliberately set low, allowing approximately 600 false detections in the entire survey, since our goal at this step was to detect all possible candidates for the subsequent maximum-likelihood fitting, in which the final decision about source significance and extent is made.

As a result of the wavelet decomposition, we obtain six images that contain detected sources of characteristic size (FWHM) approximately $7''$, $15''$, $30''$, $60''$, $120''$, and $240''$ (scales 1 through 6). We use these images to select candidate extended sources for subsequent modeling. Since the FWHM of the PSF is $25''$ on-axis, most point sources are detected on scales 1–3 and are absent at scales 4–6. On the other hand, a distant cluster with core radius of 250 kpc at $z = 0.5$ has an angular radius of $35''$ (equivalent to $\sim 70''$ FWHM) and hence is detected at scales 4–6, to which point sources do not contribute. Even clusters with smaller core radii, $\sim 10''$, would be detected at scale 4, because their surface brightness profiles become broader than $\sim 30''$ FWHM when blurred by the PSF. Therefore, cluster candidates can be selected as sources detected at scale 4 or higher. Some point sources, especially those at large off-axis angles where the angular resolution degrades, are detected at scale 4. This shows that our cluster candidate selection based on the wavelet decomposition is lenient, and we are unlikely to miss any real clusters at this step. The next step is the maximum-likelihood fitting of selected candidate extended sources to determine the significance of their extent and existence, which will be used for the final cluster selection.

3.3. Maximum-Likelihood Fitting of Sources

3.3.1. Isolated Clusters

The procedure is straightforward for isolated extended sources. The photon image is fit by a model that consists of the β-model convolved with the PSF. Source position, core radius, and total flux are free parameters, while β is fixed at a value of 0.67. The model also includes the fixed background taken from the map calculated as described in § 2. The PSF is calculated at the appropriate off-axis angle for a typical source spectrum in the 0.6–2 keV energy band (Hasinger et al. 1993a). The best fit parameters are found by minimizing $-2 \ln L$ (Cash 1979):

$$-2 \ln L = -2 \sum (d_{ij} \ln m_{ij} - m_{ij}) , \qquad (3)$$

where d_{ij} and m_{ij} are the number of photons in the data and the model in pixel (i, j), respectively, and the sum is over all
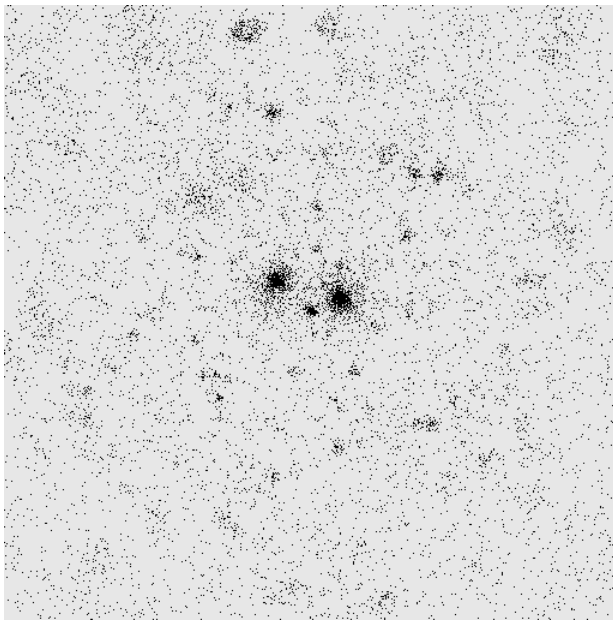
FIG. 3a
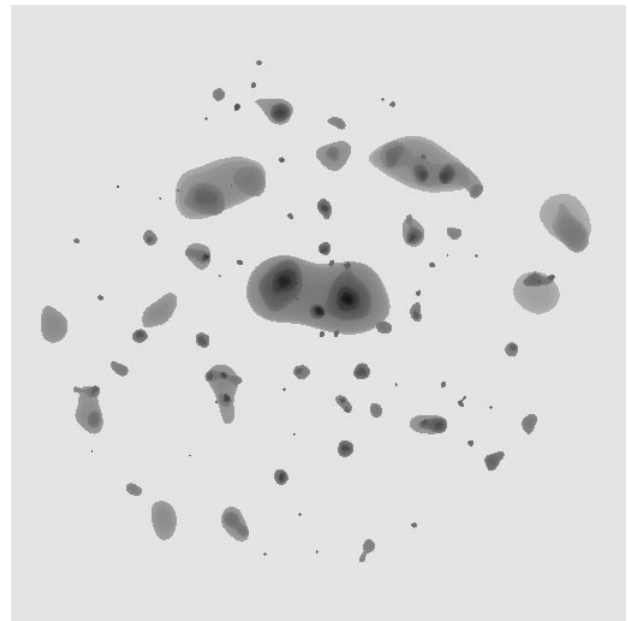
FIG. 3b
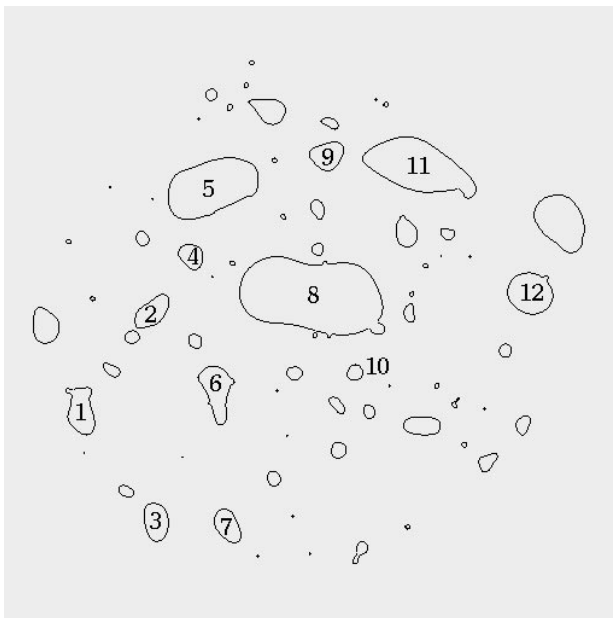
FIG. 3c
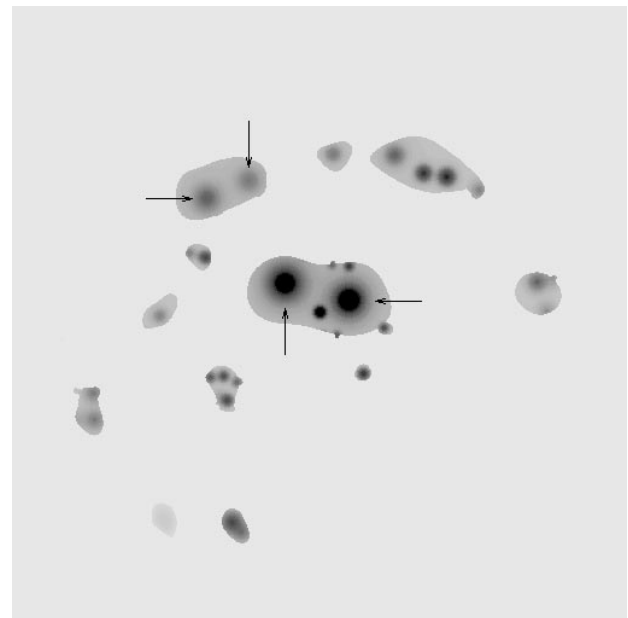
FIG. 3d

FIG. 3.—Detection of extended sources in the 1701 + 6411 field. The wavelet decomposition uses the photon image (*a*) to detect significant structures of different angular scale (*b*). (*c*) Wavelet image is split into a number of connected domains. The domains containing candidate extended sources are numbered. The best-fit image is shown in (*d*). Extended sources that passed our final selection are marked. All four sources were later confirmed as clusters by optical observations.

pixels in the fitted region. Note that m_{ij} includes background, so $-2 \ln L$ is defined even if the source flux is set to zero. Along with best-fit parameters we determine the formal significances of source existence and extent. The significance of source existence is found from the change in $-2 \ln L$ resulting from fixing the source flux at zero (Cash 1979). Similarly, the significance of the source extent is found by fixing the core radius at zero and refitting the source position and flux.

3.3.2. *Modeling of Nonisolated Clusters*

Point sources in the vicinity of the extended source must be included in the fit. We use local maxima in the combined wavelet scales 1–3 to create the list of point sources. For the fitting, point sources are modeled as the PSF calculated for a typical source spectrum as a function of off-axis angle. Point source fluxes are free parameters, but their positions are fixed because they are accurately determined by the wavelet decomposition. The fitting procedure is analogous to that for isolated extended sources.

As was discussed above, some point sources are detected at scale 4, and therefore we initially fit them as extended sources, i.e., by the β-model with free core radius and position. The best-fit core radii for such sources are small and consistent with zero, so they are not included in the final catalog. However, these sources may interfere with the

determination of significance of source extent. Suppose that a faint point source is located next to a bright cluster, and that the point source is fitted by the β-model with free position. The best-fit core radius of the point source component will be close to zero. To estimate the significance of the cluster extent, we set the core radius of the cluster component to zero and refit all other parameters, including source positions. In this case, the best-fit model will consist of the former cluster component at the position of the point source and the former point source component at the position of the cluster having nonzero core radius. The net change of $-2 \ln L$ will be zero and we will conclude that the cluster component is not significantly extended. To overcome this interference, we update source lists after the first fitting. Those extended sources that have best-fit core radii $< 5''$ are removed from the list of extended sources and added to the list of point sources. Parameters of the remaining extended sources are then refitted.

3.3.3. *Final Source Selection*

Next, we make the final selection of extended sources.

1. The main requirement is that the source must be real and significantly extended. For this, we require that the formal significance of the source existence must exceed 5 σ and the significance of its extent must be greater than 3.5 σ.

2. We find, however, that because of the nonlinearity of the model, the formal significance of the source extent is often overestimated for faint sources on top of the very low background. To exclude these cases, we required that the total source flux must exceed 25 photons.

3. Some bright sources have a small but significant intrinsic extent. An example is a bright Galactic star with a very soft spectrum. Its image is slightly broader than the PSF for hard point sources because the PSF is broader at low energies and the stars have a larger proportion of soft photons. To exclude such cases, we required that the source core radius must be greater than $\frac{1}{4}$ of the FWHM of the PSF. This requirement is met automatically for faint clusters, because faint sources with small core radii cannot be significantly extended, i.e., cannot satisfy condition (1). This third criterion sets the lower limit of $6''.25$ for core radii of clusters in our catalog. Even at $z = 1$, this angle corresponds to 50 kpc.

4. Finally, one has to exclude sources associated with the target of observation, as well as sources detected at large off-axis angles where PSF degradation makes detection of the source extent uncertain. Our last requirement is that the source is at least $2'$ from the target of the observation and at an off-axis angle smaller than $17'.5$.

Sources satisfying criteria 1–4 comprise the final catalog.

3.4. *A Real-Life Example*

To minimize computations, we fit the data only in those regions where the sum of scales 1–6 is positive, i.e., where an excess over the background is found by the wavelet decomposition. To improve the computational efficiency still further, the image is split into connected domains. Sources located within the same domain are fit simultaneously. The whole procedure of the extended source detection is illustrated in Figure 3. The raw photon image is shown in Figure 3a. The wavelet decomposition detects 97 sources in this field. The sum of scales 1–6 is shown in Figure 3b. This image is split into connected domains (Fig. 3c). Domains that contain sources detected at scales 4, 5, or 6, are numbered. The best-fit model image in these domains is shown in Figure 3d. Extended sources that passed the final selection are marked by arrows. All four of them are optically confirmed clusters. Note that the number of candidate extended sources found by the wavelet decomposition is more than 3 times the number of finally selected clusters. Thus, the selection of candidate sources by the wavelet analysis is rather lenient and does not miss real extended sources.

Using the detection procedure described in this section, we selected 239 significantly extended X-ray sources in 647 fields. In the following sections, we describe the measurement of their X-ray parameters and the optical observations and present our final catalog.

4. MEASUREMENT OF CLUSTER X-RAY PARAMETERS

For each detected cluster, we derive its position, radius, total X-ray flux, and the uncertainties in these parameters. All these quantities are derived from the best-fit β-model, and their statistical errors are determined by Monte Carlo simulations. For this, we use the best-fit model image (which includes clusters, point sources, and the background) as a template, simulate the data using Poisson scatter, and refit the simulated data. The errors are determined from the distribution of the best-fit values in 100 simulations. In this section, we discuss the measurement details and sources of additional systematic errors of the cluster parameters.

4.1. *Positional Accuracy*

Cluster position is measured as the best-fit centroid of the β-model. In addition to the statistical uncertainty of the position, there is a systematic uncertainty due to inaccuracy of the *ROSAT* aspect solution. The aspect solution errors result in a systematic offset of all X-ray sources in the field with respect to their optical counterparts. To correct this error, we examined the positional correspondence of X-ray sources and objects in the Digitized Sky Survey (DSS). If possible, targets of observations or other prominent sources (galaxies or bright stars) were used to find the precise coordinate correction. Coordinate shifts measured this way have an uncertainty of $2''–5''$, which is negligible compared to the statistical error of cluster positions. If no optical counterparts of X-ray sources were found in the DSS, we assigned a systematic position error of $17''$, the rms value of shifts measured using targets of observation. In some observations without a bright target, we found a correlation between fainter X-ray and optical sources, and measured shifts from this correlation. We regarded this shift measurement as less reliable than that using targets and assigned an intermediate systematic error of $10''$ to the cluster position in such fields. The uncertain rotation of the PSPC coordinate system results in a systematic error of $\sim 5''$ or less (Briel et al. 1996). We did not correct for the rotation, but simply added $5''$ in quadrature to the offset uncertainty. The final position error listed in Table 3 is the sum of systematic and statistical errors in quadrature.

4.2. *Core Radius*

Since it is impossible to fit the β-parameter using our data, we measure core radius for fixed $\beta = 0.67$ and refer to this value as the effective cluster radius r_e. Effective radius can be also defined as the radius at which the surface brightness falls by a factor of $2^{3/2}$ and hence is a physically meaningful combination of core radius and β. The r_e

measurement by fitting a $\beta = 0.67$ model is accurate to $\pm 20\%$ within the observed range of β, $0.6 < \beta < 0.8$ (Jones & Forman 1998).

We will now show that the radius measurement is relatively insensitive to the presence of cooling flows that cause a surface brightness excess in the central region of the cluster (see, e.g., Fabian 1994). Cooling flow clusters in general cannot be fit by the β-model. However, in distant clusters, the central excess is completely removed by the PSF blurring, and cooling flows simply reduce the core radius value. To study the possible influence of the cooling flow on the derived effective radii, we use the *ROSAT* PSPC image of Abell 2199, a nearby cluster with a moderate cooling flow of 200 $M_\odot$ yr^{-1} (Edge, Stewart, & Fabian 1992). The β-model fit for all radii yields $\beta = 0.57$, $r_c = 69$ kpc. If the inner 200 kpc region is excluded to remove the cooling flow contamination, the best-fit parameters are $\beta = 0.64$, $r_c = 137$ kpc, which corresponds to an effective radius of 142 kpc. We then determine the radius value that we would measure if A2199 were located at $z = 0.4$. At this redshift, the FWHM of the PSF corresponds to ~ 200 kpc. We convolve the image with this "PSF" and fit accounting for the smoothing and without exclusion of the center. The best-fit parameters for the smoothed data are $\beta = 0.61$, $r_c = 95$ kpc. Fixing $\beta = 0.67$, as we do for the analysis of distant clusters, we obtain $r_c = 110$ kpc, only 22% smaller than the true value obtained by excluding the cooling flow.

4.3. *X-Ray Flux*

The surface brightness of most of detected extended sources significantly exceeds the background only in a very limited area near the source center. Therefore, the total source flux simply integrated in a wide aperture has an unacceptably large statistical uncertainty. To overcome this, the flux is usually directly measured within some small aperture and then extrapolated to infinity using a reasonable model of the surface brightness profile (Henry et al. 1992; Nichol et al. 1997; Scharf et al. 1997). Similarly to this approach, we derived total fluxes from the normalization of the best-fit β-model. The most serious problem with the flux measurement using such limited-aperture photometry is the necessity to extrapolate the observed flux to infinity. This extrapolation is a potential source of large systematic errors because the surface brightness distribution at large radii is unknown. For example, consider the flux extrapolation from the inner 2.5 core radius region using β-models with different β. This inner region contains 49% of the total flux if $\beta = 0.6$, 64% if $\beta = 0.67$, and 70% if $\beta = 0.7$. Therefore, assuming $\beta = 0.67$, one underestimates the flux by $\sim 30\%$ if in fact $\beta = 0.6$, the median value in the Jones & Forman (1998) sample. In addition, a trend of β with cluster redshift or luminosity will introduce systematic changes within the sample. For example, Jones & Forman find that lower luminosity clusters have smaller β, which might result in underestimation of their fluxes.

To address the issue of systematic flux errors in more detail, we have used simulated realistic data (§ 7) to estimate the effect of the assumed value of β on the cluster flux determination. Clusters were fit as described in § 3.3, but for three different values of β, 0.6, 0.67, and 0.7. Dashed lines in Figure 4 show average ratios of the measured and input total flux as a function of the true β if the flux is measured as a normalization of the best-fit model with β fixed at 0.6 and 0.7. In all cases, significant biases are present over the
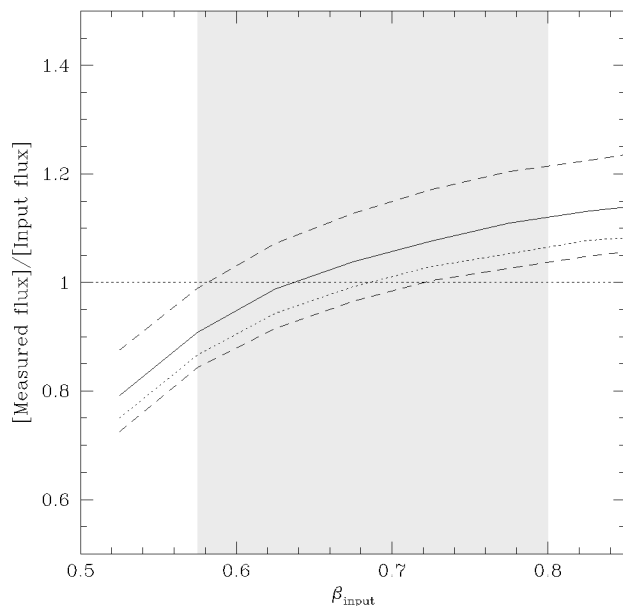
FIG. 4.—Ratio of the measured and input cluster flux as a function of the cluster β. Fluxes of simulated clusters were measured by fitting β-models with β fixed at 0.6 (*upper dashed line*), 0.7 (*lower dashed line*), and 0.67 (*dotted line*). Solid line corresponds to the flux measure $(f_{0.6} + f_{0.7})/2$ used for our sample.

observed range of β (Jones & Forman 1998; Fig. 4, *shaded region*). We are interested in a flux measure that has the smallest uncertainty for the whole range of β, not the one that yields an unbiased flux estimate for some fixed value of β. The quantity $(f_{0.6} + f_{0.7})/2$, where $f_{0.6}$ and $f_{0.7}$ are cluster fluxes calculated assuming $\beta = 0.6$ and 0.7, respectively, is close to the desired flux measure (solid line in Fig. 4). It provides a satisfactory flux estimate, accurate to $\pm 10\%$ over the observed range of β. We use this quantity to measure cluster fluxes throughout the rest of this paper and add the systematic error of 10% to the statistical uncertainty in the flux.

Our sample includes four EMSS clusters (Henry et al. 1992), which were also detected in the WARPS survey (Jones et al. 1998) and whose *ROSAT* observations were studied by Nichol et al. (1997). We use these clusters to compare fluxes from all these surveys. Table 1 shows general agreement, within 10%, between different *ROSAT* surveys, especially between ours and WARPS. However, Henry et al. and, to a smaller degree, Nichol et al. find fluxes that are systematically lower than those from our survey and WARPS. Note that all *ROSAT* surveys use essentially the same data, so the difference cannot be explained by statistical fluctuations. Jones et al. have earlier performed a similar comparison using a larger number of clusters. They also noted the systematic difference of their fluxes compared to EMSS and Nichol et al. and explained this by the difference in flux measurement methods. All the surveys derived fluxes by extrapolation from that measured within some aperture using a β-model. However, Henry et al. and Nichol et al. assumed fixed $\beta = 0.67$ and $r_c = 250$ kpc, while Jones et al. estimated core radii individually for each cluster, similar to our procedure. Also, our fluxes can be $\sim 5\%$ higher than those obtained for $\beta = 0.67$ because our measurements are optimized for the entire observed range of β. Cluster-to-cluster variations of β probably explain $\sim 10\%$ nonsystematic differences in flux for the same cluster in

TABLE 1

COMPARISON OF FLUX MEASUREMENTS

CLUSTER	z	OUR SURVEY (0.5–2 keV)	EMSS (0.3–3.5 keV)	NICHOL ET AL. (0.3–3.5 keV)	WARPS (0.5–2 keV)	FLUX RATIO[a]		
						EMSS	Nichol et al.	WARPS
MS 1201.5+2824......	0.167	102.6	169.4	174.7	95.6	1.03	1.00	1.07
MS 1208.7+3928......	0.340	26.6	41.1	42.7	29.3	1.12	1.08	0.91
MS 1308.8+3244......	0.245	46.7	69.3	74.9	50.7	1.16	1.07	0.92
MS 2255.7+2039......	0.288	50.5	57.6	73.9	51.9	1.53	1.19	0.97
Average................						1.21	1.09	0.97

NOTE.—All fluxes are in units of 10^{-14} ergs s^{-1} cm^{-2}.

[a] Ratios of fluxes measured in our survey and EMSS, Nichol et al. 1997, and WARPS. To calculate these ratios, 0.3–3.5 keV fluxes were converted to the 0.5–2 keV energy band using the conversion coefficients from Jones et al. 1998.

different surveys. Jones et al. also compared their measurements with fluxes directly integrated in a 4 Mpc aperture. They found that their fluxes exceed the directly measured values by 10%, with $\sim 60\%$ of that difference explained by the cluster luminosity originating from outside 4 Mpc. Since our measurements are $\sim 3\%$ lower than those of Jones et al., we conclude that our fluxes are accurate within a few percent, which is better than the assigned systematic uncertainty.

5. OPTICAL OBSERVATIONS

We are carrying on a program of optical photometric and spectroscopic observations of our clusters. A complete discussion of optical observations and data reduction will be presented in McNamara et al. (1998). Below, we discuss the optical results relevant to the X-ray catalog presented here.

5.1. Cluster Identification

In some earlier works, optical identification of X-ray selected clusters seeks a concentration of galaxies in redshift space, which requires a large investment of telescope time. For our sources, the detected extended X-ray emission is already a strong indication of cluster existence. Therefore, we relaxed the optical identification criteria and required that either a significant enhancement in the projected density of galaxies be found or that an elliptical galaxy not included in the NGC catalog lie at the peak of the X-ray emission. While the galaxy concentration criterion is obvious, the elliptical galaxy one is needed to identify poor clusters and groups that fail to produce a significant excess of galaxies over the background. It also helps to identify "fossil groups," in which galaxies have merged into a cD (Ponman et al. 1994). A potential problem with this second criterion is that an active nucleus of an elliptical galaxy might be falsely identified as a cluster. However, a significant extent of X-ray emission in all our sources makes this unlikely. Also, our spectroscopic observations of such single-galaxy sources never showed emission lines characteristic of AGNs.

We obtained R-, and in some cases I-, V-, and B-band CCD images on the Fred Lawrence Whipple Observatory 1.2 m, Danish 1.54 m, and Las Campanas 1 m telescopes. For brighter clusters, we also used second generation Digitized Sky Survey (DSS-II) plates. Using the DSS-II, it is possible to identify clusters at $z \lesssim 0.45$. The sensitivity of our CCD images is adequate to identify clusters to $z = 0.7$–0.9. If no cluster was visible in the CCD image, we considered this object as a false detection (although it could be a very distant cluster). These objects were retained in

the sample for statistical completeness but are marked in Table 3.

We also searched for possible optical counterparts in the NASA Extragalactic Database (NED). The summary of NED identifications is given in Table 2. We obtained CCD photometry for some of the catalogued clusters and tried to obtain spectroscopic data if redshifts were not available. Fifteen extended sources were identified with isolated NGC galaxies and therefore removed from the cluster catalog. One object, identified with an AGN, was considered as a false detection but was left in the catalog for statistical completeness.

A summary of optical identifications of our cluster catalog is given in Table 2. In total, we confirmed 91% of sources as clusters in the total sample, while 9% of sources are likely false detections. One object was not identified because its optical images are saturated by neighboring Arcturus. In the X-ray bright subsample, $f > 2 \times 10^{-13}$ ergs s^{-1} cm^{-2}, we optically confirmed 98% of sources as clusters. These high success rates demonstrate the high quality of our X-ray selection.

5.2. Spectroscopic and Photometric Redshifts

We observed an incomplete subsample of clusters spectroscopically on the Multiple Mirror Telescope (MMT) and the ESO 3.6 m and Danish 1.54 m telescopes. In most cases, we identified several obvious cluster galaxies in the CCD images and then obtained long-slit spectra, usually for 2–3

TABLE 2

STATUS OF OPTICAL IDENTIFICATIONS

Description	Number
Total sample	
Objects..	223
Confirmed clusters..	203
False X-ray detections	19
No CCD imaging data......................................	1
NED identifications	
Previously known clusters	37
Previously known clusters with measured redshifts......	29
NED AGN	1
X-ray flux $> 2 \times 10^{-13}$ ergs s^{-1} cm^{-2}	
Objects..	82
Confirmed clusters..	80
False detections	1
No data	1

galaxies per cluster. The slit always included the brightest cluster galaxy. For 10 clusters observed at the ESO 3.6 m telescope, we obtained multiobject spectra, 10–15 galaxies per cluster. Altogether, we measured 47 redshifts ranging from $z = 0.040$ to $z = 0.574$. Further details of spectroscopic observations will be presented in McNamara et al. (1998).

For those clusters without spectroscopic data, we estimated redshifts from the magnitude of the brightest cluster galaxy (BCG). The BCG was selected as the brightest galaxy either within the error circle of the cluster X-ray position or the one in the center of the galaxy concentration; both criteria were met simultaneously in most cases. Although the BCG selection was somewhat subjective, the tightness of the magnitude versus redshift relation obtained for $\sim\frac{1}{4}$ of the total sample confirms our procedures. For nearby clusters, the scatter in the absolute magnitude of BCGs is small, $\sigma_M \approx 0.2$ (Sandage 1972), which corresponds to $\approx 10\%$ distance error. Our results show that the scatter is small at higher redshifts as well. The magnitude versus redshift relation is calibrated within our sample, and photometric redshifts are estimated using the CCD images obtained under photometric conditions or DSS-II plates.

The CCD galaxy photometry was performed in the R-band. The BCG magnitudes were measured within a fixed $4''$ aperture. Such an aperture was chosen to make the measurement relatively insensitive to poor seeing, which was $\sim 2''$ in some cases, and encompass $\sim 50\%$ of light in high-redshift galaxies. The fixed angular aperture corresponds to the metric aperture increasing with redshift, from 10 kpc at $z = 0.1$ to 29 kpc at $z = 0.5$. The increase of the metric aperture is a monotonic function of redshift, the same for all clusters, and thus does not prevent us from using the m-z relation for photometric redshift estimates. We did not make K-corrections of BCG magnitudes because this is also a monotonic systematic function of redshift. Measured magnitudes were corrected for Galactic extinction using Burstein & Heiles (1982) maps.

There is a correlation between the BCG magnitude and the cluster X-ray luminosity (Hudson & Ebeling 1997), which increases the scatter in the m-z relation. Within our sample, the absolute BCG magnitude changes approximately as $-0.5 \log L_X$, in good agreement with the Hudson & Ebeling results. Below, we use the corresponding correction, $m' = m + 0.5 \log (L_X/10^{44} \, \mathrm{ergs}^{-1})$, to compensate for this effect.

The X-ray luminosity–corrected BCG magnitude is plotted versus cluster redshift in Figure 5. This dependence can be well fit by a cosmological dimming law $m' = m_0 + 5 \log z - 1.086(q' - 1)z$ with best-fit parameters $m_0 = 20.45$ mag and $q' = -0.121$. In this equation, q' provides a useful parametrization but does not have the meaning of the cosmological deceleration parameter because magnitudes were not K-corrected and a varying metric aperture was used. The best-fit relation is shown by the dotted line in Figure 5. Photometric redshifts were estimated from the analytical fit using the following iterative procedure. We estimated redshift from the uncorrected BCG magnitude. Using the estimated redshift, we calculated the X-ray luminosity, corrected the BCG magnitude as described above, and reestimated z. The process was repeated until the estimated redshift converged. We checked this procedure by estimating photometric redshifts of clusters with measured redshifts. This comparison has shown that the photometric estimate is unbiased and has an uncertainty of $\Delta z = ^{+0.04}_{-0.07}$.

We also observed five high-z EMSS clusters ($0302 + 1658$, $0451.6 - 0305$, $0015.9 + 1609$, $1137.5 + 6625$, and $1054.5 - 0321$) to check the m-z relation at high redshift using an external X-ray selected sample. These clusters are plotted as crosses in Figure 5. They follow the relation defined by our sample very well. In addition, these five EMSS clusters are very X-ray luminous; their accordance with the m-z relation confirms the validity of the X-ray luminosity correction we apply to BCG magnitudes.

For 7 clusters without photometric CCD data, redshifts were estimated using the Second Digitized Sky Survey
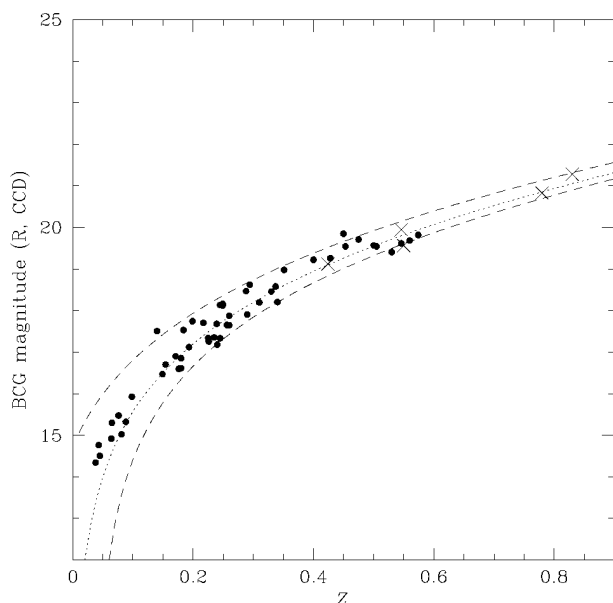
FIG. 5a
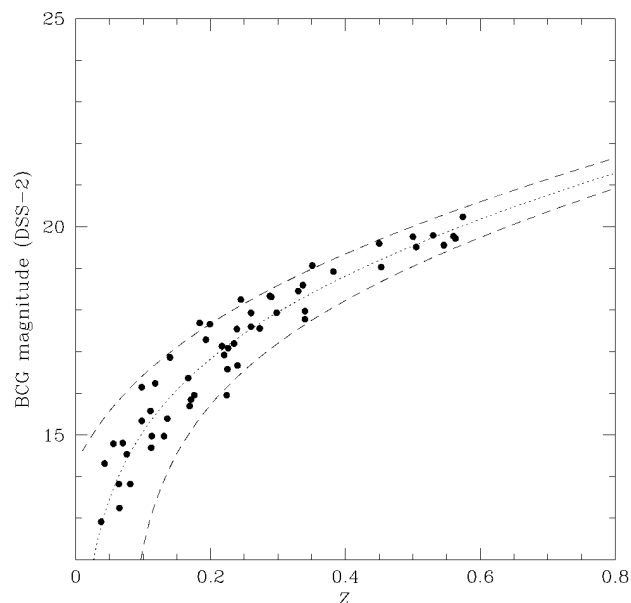
FIG. 5b

FIG. 5.—(a) X-ray luminosity–corrected BCG magnitudes vs. redshift. The dotted line shows the analytical fit (see text). The estimated redshift uncertainty of $\Delta z = ^{+0.04}_{-0.07}$ is shown by dashed lines. Crosses mark five high-redshift EMSS clusters. These clusters were not used in the fit. (b) Same as (a), but magnitudes were measured using DSS-II. The dotted line shows the best-fit relation, and the dashed lines correspond to $\Delta z = \pm 0.07$.

TABLE 3

CLUSTER CATALOG

Number (1)	R.A. (J2000) (2)	decl. (J2000) (3)	F_X (10^{-14} cgs) (4)	δF_X (10^{-14} cgs) (5)	r_c (arcsec) (6)	δr_c (arcsec) (7)	z (8)	$z_{min} - z_{max}$ (9)	δr (arcsec) (10)	Note (11)
1	00 30 33.2	+26 18 19	24.3	3.0	31	3	0.500		13	
2	00 41 10.3	−23 39 33	9.8	2.4	25	12	0.15	0.08–0.22[dss]	19	
3	00 50 59.2	−09 29 12	36.6	4.9	45	4	0.21	0.14–0.25	11	
4	00 54 02.8	−28 23 58	10.8	1.5	37	6	0.25	0.18–0.29	16	
5	00 56 55.8	−22 13 53	25.9	5.2	61	12	0.11	0.04–0.18[dss]	17	
6	00 56 56.1	−27 40 12	6.9	0.8	14	2	0.563		13	1
7	00 57 24.2	−26 16 45	186.1	21.3	82	6	0.113		14	2
8	01 10 18.0	+19 38 23	7.8	1.6	35	8	0.24	0.17–0.28	16	
9	01 11 36.6	−38 11 12	8.9	1.7	18	3	0.122		9	
10	01 22 35.9	−28 32 03	26.9	6.3	37	16	0.24	0.17–0.28	14	3
11	01 24 35.1	+04 00 49	7.5	2.2	31	14	0.27	0.20–0.31	20	
12	01 27 27.8	−43 26 13	5.7	1.9	34	13			19	F
13	01 28 36.9	−43 24 57	7.5	1.3	10	3	0.26	0.19–0.30	9	
14	01 32 54.7	−42 59 52	32.3	8.1	75	25	0.088		23	4
15	01 36 24.2	−18 11 59	4.8	1.0	21	8	0.25	0.18–0.29	15	
16	01 39 39.5	+01 19 27	10.9	2.0	37	8	0.25	0.18–0.29	12	
17	01 39 54.3	+18 10 00	27.3	3.8	33	5	0.176		9	5
18	01 42 50.6	+20 25 16	26.1	4.5	29	6	0.43	0.36–0.47	22	
19	01 44 29.1	+02 12 37	10.1	2.3	32	11	0.15	0.08–0.19	13	
20	01 54 14.8	−59 37 48	14.5	3.2	22	7	0.360		12	
21	01 59 18.2	+00 30 12	32.7	4.1	13	2	0.26	0.19–0.30	9	
22	02 06 23.4	+15 11 16	13.0	2.5	53	10	0.27	0.20–0.31	14	
23	02 06 49.5	−13 09 04	26.0	4.4	28	8	0.31	0.24–0.35	15	
24	02 10 13.8	−39 32 51	4.6	1.1	22	10	0.19	0.12–0.23	11	
25	02 10 25.6	−39 29 47	6.4	1.3	28	9	0.27	0.20–0.30	14	
26	02 28 13.2	−10 05 40	24.4	3.9	35	6	0.149		15	
27	02 36 05.2	−52 25 03	5.8	1.2	16	4			9	F
28	02 37 59.2	−52 24 40	64.4	8.2	49	8	0.16	0.09–0.20	14	6
29	02 39 52.6	−23 20 35	8.4	1.8	51	14	0.49	0.42–0.53	23	
30	02 58 46.1	+00 12 44	10.8	2.9	28	7	0.23	0.16–0.27	19	
31	02 59 33.9	+00 13 47	32.4	5.2	42	11	0.17	0.10–0.21	12	
32	03 22 20.1	−49 18 40	40.3	7.2	69	11	0.067		15	7
33	03 37 44.9	−25 22 39	3.7	0.7	7	2	0.38	0.31–0.42	8	
34	03 41 57.1	−45 00 11	1.7	0.4	27	9	0.44	0.37–0.48	12	
35	03 51 37.8	−36 49 50	8.8	2.2	31	17	0.29	0.22–0.33	24	
36	04 28 43.0	−38 05 54	20.8	5.0	54	13	0.154		20	8
37	04 34 15.7	−08 31 17	7.2	2.2	25	14	0.24	0.17–0.28	24	
38	05 05 57.8	−28 25 47	14.2	1.9	25	4	0.131		15	
39	05 06 03.7	−28 40 44	19.5	3.4	84	20	0.14	0.07–0.18	21	
40	05 21 10.7	−25 30 44	17.6	4.0	37	13	0.60	0.53–0.64	15	
41	05 22 14.2	−36 25 04	18.4	3.8	16	5	0.53	0.46–0.57	9	
42	05 28 40.3	−32 51 38	19.9	2.5	26	3	0.273		8	
43	05 29 38.4	−58 48 10	5.6	1.0	10	3	0.58	0.51–0.62	9	
44	05 32 43.7	−46 14 11	41.1	4.3	12	1	0.13	0.06–0.17	7	
45	05 33 53.2	−57 46 52	22.2	6.1	81	28	0.18	0.11–0.22	37	
46	05 33 55.9	−58 09 16	9.0	2.8	53	20	0.17	0.10–0.21	30	
47	08 10 23.9	+42 16 24	238.6	27.2	59	5	0.064		14	
48	08 18 57.8	+56 54 34	10.1	2.5	29	9	0.260		17	
49	08 19 22.6	+70 54 48	10.1	1.8	24	6	0.226		15	
50	08 19 54.4	+56 34 35	30.8	5.0	16	5	0.260		14	
51	08 20 26.4	+56 45 22	22.9	4.2	39	14	0.043		18	
52	08 26 06.4	+26 25 47	10.9	2.6	59	19	0.351		22	
53	08 26 29.7	+31 25 15	11.1	4.7	47	22	0.26	0.19–0.30	31	
54	08 31 16.0	+49 05 06	12.3	4.0	30	15			17	F
55	08 34 27.4	+19 33 24	8.3	1.7	31	7			18	F
56	08 41 07.4	+64 22 43	29.1	3.2	35	3	0.36	0.29–0.40	8	
57	08 41 43.4	+70 46 53	8.9	2.1	31	12	0.235		13	
58	08 42 52.8	+50 23 16	6.3	1.7	23	10	0.48	0.41–0.53	16	
59	08 47 11.3	+34 49 16	12.2	3.0	28	9	0.560		17	
60	08 48 47.6	+44 56 21	3.3	0.6	14	4	0.574		13	
61	08 48 56.3	+44 52 16	2.7	0.6	23	6			14	F
62	08 49 11.1	+37 31 25	14.7	3.0	36	10	0.240		14	
63	08 52 33.6	+16 18 08	37.1	6.2	33	10	0.098		19	
64	08 53 14.1	+57 59 39	19.8	5.8	35	14	0.475		17	
65	08 57 45.7	+27 47 32	6.8	1.6	42	11	0.50	0.43–0.54	27	
66	08 58 25.0	+13 57 16	6.4	1.0	14	5	0.54	0.47–0.58	10	
67	09 07 17.9	+33 30 09	4.4	0.8	24	5	0.46	0.39–0.49	14	
68	09 07 20.4	+16 39 09	148.5	17.6	55	5	0.076		9	9
69	09 10 39.7	+42 48 41	8.3	2.0	76	23	...	...	24	U
70	09 21 13.4	+45 28 50	23.9	4.7	26	5	0.337		11	
71	09 26 36.6	+12 42 56	16.7	2.1	16	3	0.50	0.43–0.54	9	

TABLE 3—*Continued*

Number (1)	R.A. (J2000) (2)	decl. (J2000) (3)	F_X (10^{-14} cgs) (4)	δF_X (10^{-14} cgs) (5)	r_c (arcsec) (6)	δr_c (arcsec) (7)	z (8)	$z_{min} - z_{max}$ (9)	δr (arcsec) (10)	Note (11)
72	09 26 45.6	+12 34 07	11.7	3.5	60	22			41	F
73	09 43 32.2	+16 40 02	23.1	3.7	36	5	0.256		10	
74	09 43 44.7	+16 44 20	21.2	4.1	69	13	0.180		17	
75	09 47 45.8	+07 41 18	13.5	3.7	32	10	0.59	0.52–0.63	17	
76	09 51 47.0	−01 28 33	7.1	1.9	25	11	0.53	0.46–0.57	22	
77	09 52 08.7	−01 48 18	9.3	2.5	39	14			18	F
78	09 53 31.2	+47 58 57	13.0	5.2	41	20			20	F, 10
79	09 56 03.4	+41 07 14	15.6	3.3	13	6	0.73	0.66–0.77	13	
80	09 57 53.2	+65 34 30	9.4	1.7	19	5	0.530		12	
81	09 58 13.5	+55 16 01	48.2	7.1	67	14	0.20	0.12–0.23	15	11
82	09 59 27.7	+46 33 57	10.5	5.2	37	23			31	F
83	10 02 40.4	−08 08 46	8.6	2.1	29	7	0.62	0.55–0.66	12	
84	10 10 14.7	+54 30 18	21.0	2.9	20	4	0.045		14	12
85	10 11 05.1	+53 39 27	4.7	1.2	23	9	0.30	0.23–0.34	11	
86	10 11 26.0	+54 50 08	20.0	5.1	94	22	0.294		24	
87	10 13 38.4	+49 33 07	45.6	9.8	107	21	0.17	0.10–0.21	22	
88	10 15 08.5	+49 31 32	10.8	2.6	14	8	0.45	0.38–0.49	10	
89	10 33 51.9	+57 03 10	14.5	4.3	24	9	0.06	0.00–0.10	16	
90	10 36 11.3	+57 13 31	18.8	3.9	15	6	0.31	0.24–0.35	13	
91	10 48 00.1	−11 24 07	18.5	3.6	35	7	0.065		19	
92	10 49 02.7	+54 24 00	9.1	1.6	22	9	0.20	0.13–0.24	12	
93	10 53 18.4	+57 20 47	2.5	0.3	12	3	0.340		8	13
94	10 56 12.6	+49 33 11	12.9	1.9	64	15	0.199		23	
95	10 58 13.0	+01 36 57	129.5	19.3	113	13	0.038		15	14
96	11 17 12.0	+17 44 24	12.0	5.6	65	33	0.51	0.44–0.55	26	
97	11 17 26.1	+07 43 35	6.1	1.6	18	7	0.40	0.33–0.44	12	
98	11 17 30.2	+17 44 44	14.4	2.5	36	10	0.63	0.56–0.67	16	
99	11 19 43.5	+21 26 44	5.5	0.9	12	3	0.11	0.04–0.15	9	
100	11 20 57.9	+23 26 41	21.3	5.0	29	8	0.71	0.64–0.75	16	
101	11 23 10.2	+14 09 44	18.2	4.9	49	24	0.32	0.25–0.36	27	
102	11 24 03.8	−17 00 11	10.8	3.4	34	19	0.41	0.34–0.45	22	
103	11 24 36.9	+41 55 59	40.1	9.6	110	30	0.18	0.11–0.22	31	
104	11 35 54.5	+21 31 05	17.8	4.0	72	20	0.14	0.07–0.18	17	
105	11 38 43.9	+03 15 38	15.9	3.7	18	6	0.14	0.07–0.18	10	
106	11 42 04.6	+21 44 57	45.9	17.4	56	34	0.18	0.11–0.22	26	
107	11 46 26.9	+28 54 15	39.2	5.8	79	11	0.17	0.10–0.21	18	
108	11 51 40.3	+81 04 38	3.7	1.1	27	7	0.27	0.20–0.31	14	
109	11 58 11.7	+55 21 45	4.7	1.0	21	5	0.15	0.08–0.19	9	
110	11 59 51.2	+55 31 56	74.2	7.6	24	2	0.081		7	15
111	12 00 49.7	−03 27 31	18.5	2.6	29	5	0.39	0.32–0.42	10	
112	12 04 04.0	+28 07 08	102.6	11.4	32	3	0.167		7	16
113	12 04 22.9	−03 50 55	8.7	1.3	26	6	0.22	0.15–0.26	14	
114	12 06 33.5	−07 44 28	129.0	16.3	64	7	0.12	0.05–0.16	15	
115	12 11 15.3	+39 11 38	26.6	3.8	14	4	0.340		8	17
116	12 13 35.3	+02 53 26	14.3	3.0	27	9	0.39	0.32–0.43	13	
117	12 16 19.4	+26 33 26	15.4	4.2	15	6	0.428		15	
118	12 18 29.1	+30 11 46	5.3	1.4	18	9	0.33	0.26–0.37	11	
119	12 21 24.5	+49 18 13	20.6	4.6	34	8	0.70	0.64–0.74	18	
120	12 22 32.5	+04 12 02	6.3	1.6	15	7			12	F
121	12 36 31.4	+00 51 43	4.8	1.2	28	8	0.17	0.10–0.21	14	
122	12 37 25.1	+11 41 27	10.6	3.4	41	15	...	...	21	U
123	12 37 38.6	+26 32 23	7.0	2.3	31	12	0.28	0.21–0.33	14	
124	12 52 05.4	−29 20 46	21.7	4.2	46	11	0.17	0.10–0.21	13	
125	12 52 11.3	−29 14 59	8.7	1.6	11	5			8	F
126	12 54 38.3	+25 45 13	10.2	2.0	31	7	0.193		13	
127	12 54 53.6	+25 50 55	13.2	2.5	40	8	0.23	0.16–0.27	12	
128	12 56 04.9	+25 56 52	9.9	1.9	30	7	0.17	0.10–0.21	11	
129	12 56 39.4	+47 15 19	5.7	0.8	25	5	0.40	0.33–0.44	10	
130	13 01 43.6	+10 59 33	28.1	5.6	54	11	0.30	0.23–0.34	18	
131	13 09 55.6	+32 22 31	9.0	2.9	42	19	0.290		23	
132	13 11 12.8	+32 28 58	46.7	5.8	22	3	0.245		8	18
133	13 11 30.2	−05 51 26	13.7	2.4	36	6	0.49	0.42–0.53	20	
134	13 25 14.9	+65 50 29	10.1	3.1	54	21	0.180		28	
135	13 25 43.9	−29 43 51	7.7	2.7	43	11			17	F
136	13 29 27.3	+11 43 31	97.0	16.6	120	16	0.023		22	19
137	13 34 31.1	−08 22 29	5.2	1.1	13	5			10	F
138	13 34 34.4	+37 56 58	1.6	0.3	16	5	0.308		11	20
139	13 35 03.7	+37 50 00	2.9	0.4	21	4	0.382		9	21
140	13 36 42.1	+38 37 32	5.9	1.6	20	9	0.180		16	
141	13 37 48.3	+48 15 46	7.1	1.5	16	4			10	F
142	13 37 50.4	+26 38 49	9.6	2.1	21	6	0.28	0.21–0.33	12	
143	13 37 53.3	+38 54 09	14.3	3.6	32	9	0.29	0.22–0.33	17	

TABLE 3—*Continued*

Number (1)	R.A. (J2000) (2)	decl. (J2000) (3)	F_X (10^{-14} cgs) (4)	δF_X (10^{-14} cgs) (5)	r_c (arcsec) (6)	δr_c (arcsec) (7)	z (8)	$z_{min} - z_{max}$ (9)	δr (arcsec) (10)	Note (11)
144......	13 40 33.5	+40 17 47	16.1	2.5	19	5	0.171		10	22
145......	13 40 53.7	+39 58 11	34.4	6.9	66	16	0.169		19	23
146......	13 41 51.7	+26 22 54	814.0	84.6	103	4	0.070		8	24
147......	13 42 05.0	+52 00 37	12.4	1.9	10	4			13	F
148......	13 42 49.1	+40 28 11	7.4	2.0	15	6	0.53	0.46–0.57	16	
149......	13 43 25.0	+40 53 14	12.6	2.8	18	7	0.140		10	
150......	13 43 29.0	+55 47 17	17.5	2.8	109	17	0.11	0.04–0.18^{dss}	23	
151......	13 54 16.9	−02 21 47	14.5	2.6	27	4	0.49	0.42–0.53	11	
152......	13 54 49.1	+69 17 20	6.4	1.9	26	10	0.18	0.11–0.22	15	
153......	14 06 16.3	+28 30 52	8.5	1.2	14	4	0.546		9	
154......	14 06 54.9	+28 34 17	25.7	3.2	30	3	0.118		8	
155......	14 10 12.4	+59 42 40	33.5	5.1	38	12	0.249		18	
156......	14 10 15.2	+59 38 31	20.1	8.7	31	22	0.249		17	25
157......	14 15 37.9	+19 06 33	25.4	3.4	52	5	...	...	13	26
158......	14 16 28.7	+44 46 41	40.4	5.2	16	4	0.400		8	
159......	14 18 31.1	+25 10 50	75.6	7.8	33	1	0.24	0.17–0.28	7	
160......	14 18 45.2	+06 44 02	16.4	3.0	18	5			9	F
161......	14 19 23.5	+06 38 42	13.1	1.9	17	4	0.61	0.54–0.65	9	
162......	14 19 57.2	+06 34 26	10.3	2.1	35	7	0.61	0.54–0.65	15	
163......	14 29 38.1	+42 34 25	8.5	2.4	35	12	0.30	0.23–0.34	26	
164......	14 38 55.5	+64 23 44	26.2	3.6	103	11	...	...	19	U
165......	14 44 07.7	+63 44 58	17.4	3.2	26	9	0.298		15	27
166......	15 00 02.7 /comm	+22 33 51	14.5	4.5	37	17	0.21	0.14–0.25	24	
167......	15 00 51.5	+22 44 41	17.8	4.2	31	10	0.450		16	
168......	15 15 32.5	+43 46 39	34.6	9.7	60	19	0.26	0.19–0.30	18	
169......	15 15 36.8	+43 50 50	10.5	3.8	34	18	0.14	0.07–0.18	22	
170......	15 24 40.3	+09 57 39	30.4	4.1	26	3	0.11	0.04–0.15	9	28
171......	15 37 44.3	+12 00 26	26.4	7.4	84	26	0.15	0.08–0.19	30	
172......	15 40 53.3	+14 45 34	7.6	2.0	17	8	0.45	0.38–0.49	13	
173......	15 44 05.0	+53 46 27	9.7	2.2	35	11	0.33	0.26–0.37	19	
174......	15 47 20.7	+20 56 50	25.4	7.0	51	20	0.23	0.17–0.28	24	
175......	15 52 12.3	+20 13 45	49.5	6.0	59	7	0.136		9	
176......	16 06 42.5	+23 29 00	12.1	2.8	34	13	0.310		12	
177......	16 20 22.0	+17 23 05	20.8	3.7	35	8	0.112		12	
178......	16 29 46.1	+21 23 54	25.3	4.0	46	8	0.184		19	
179......	16 30 15.2	+24 34 59	179.4	25.9	129	13	0.09	0.02–0.13	23	29
180......	16 31 04.6	+21 22 02	29.1	6.4	58	14	0.098		16	
181......	16 33 40.0	+57 14 37	3.5	0.7	24	8	0.239		14	
182......	16 39 55.6	+53 47 56	130.5	14.8	170	8	0.111		12	30
183......	16 41 10.0	+82 32 27	80.5	10.9	78	11	0.26	0.19–0.30	13	31
184......	16 41 52.5	+40 01 29	29.4	7.8	51	15	0.51	0.44–0.55	24	
185......	16 42 33.5	+39 59 05	5.3	1.4	19	9			12	F, 32
186......	16 42 38.9	+39 35 53	10.1	2.3	27	9	0.47	0.40–0.51	16	
187......	16 58 34.7	+34 30 12	33.6	5.2	58	10	0.330		16	
188......	16 59 44.6	+34 10 17	9.8	3.4	25	11	0.32	0.25–0.36	16	
189......	17 00 42.3	+64 13 00	45.6	4.7	18	1	0.225		7	33
190......	17 01 23.0	+64 14 11	38.6	4.2	25	2	0.453		7	
191......	17 01 46.1	+64 21 15	3.5	0.7	32	8	0.220		14	
192......	17 02 13.3	+64 20 00	6.3	1.2	32	7	0.224		12	
193......	17 22 53.8	+41 05 25	29.4	6.5	42	12	0.33	0.26–0.37	22	
194......	17 29 01.9	+74 40 46	17.3	7.2	100	31	0.28	0.21–0.35^{dss}	40	
195......	17 46 29.1	+68 48 54	22.3	3.2	56	10	0.217		13	
196......	20 03 28.4	−55 56 47	47.6	6.3	16	2	0.015		8	34
197......	20 04 49.4	−56 03 44	10.4	2.5	30	11	0.71	0.64–0.78^{dss}	16	
198......	20 05 13.6	−56 12 58	35.0	4.9	7	3			9	F
199......	20 59 55.2	−42 45 33	11.2	1.8	9	3	0.47	0.40–0.51	8	
200......	21 08 51.2	−05 16 49	11.6	1.7	34	7	0.30	0.23–0.34	12	
201......	21 14 20.4	−68 00 56	25.8	3.3	17	3	0.15	0.08–0.19	13	
202......	21 37 06.7	+00 26 51	27.8	5.7	55	20	0.05	0.00–0.12^{dss}	21	35
203......	21 39 58.5	−43 05 14	8.3	2.0	12	6	0.30	0.23–0.34	15	
204......	21 46 04.8	+04 23 19	13.8	2.1	17	2	0.531		13	
205......	22 02 44.9	−19 02 10	6.6	2.2	36	9	0.34	0.27–0.38	22	
206......	22 12 38.2	−17 13 55	5.4	1.4	22	13	0.12	0.05–0.16	12	
207......	22 13 31.0	−16 56 11	18.1	3.2	41	12	0.32	0.25–0.36	17	
208......	22 39 24.7	−05 47 04	22.2	3.5	11	2	0.245		13	36
209......	22 39 34.4	−06 00 14	5.9	2.0	21	10	0.15	0.08–0.19	19	
210......	22 39 38.9	−05 43 18	32.4	5.0	34	5	0.245		15	37
211......	22 47 29.1	+03 37 13	23.0	6.3	46	17	0.18	0.11–0.22	20	
212......	22 57 49.4	+20 56 25	11.1	2.1	22	7	0.28	0.21–0.32	11	
213......	22 58 07.1	+20 55 07	50.5	6.1	24	3	0.288		9	38
214......	23 05 26.2	−35 46 01	15.5	3.4	55	14	0.21	0.14–0.25	15	

TABLE 3—*Continued*

Number (1)	R.A. (J2000) (2)	decl. (J2000) (3)	F_X $(10^{-14}$ cgs) (4)	δF_X $(10^{-14}$ cgs) (5)	r_c (arcsec) (6)	δr_c (arcsec) (7)	z (8)	$z_{min} - z_{max}$ (9)	δr (arcsec) (10)	Note (11)
215......	23 05 26.6	−51 30 30	4.2	1.4	21	10	0.21	0.14–0.25	17	
216......	23 18 04.8	−42 35 30	15.5	2.7	28	8	0.27	0.20–0.31	17	
217......	23 19 33.9	+12 26 17	38.2	4.7	30	6	0.25	0.18–0.29	10	
218......	23 25 39.1	−54 43 59	22.4	7.7	91	26	0.10	0.03–0.14	35	
219......	23 28 49.9	+14 53 12	7.6	1.7	27	12	0.49	0.42–0.54	21	
220......	23 31 52.1	−37 47 11	10.8	4.7	46	25	0.26	0.18–0.29	28	
221......	23 48 53.7	−31 17 20	32.5	5.1	43	8	0.21	0.14–0.28[dss]	12	39
222......	23 49 07.6	−31 22 26	6.0	1.4	21	6			11	F
223......	23 55 11.8	−15 00 26	26.6	6.7	70	20	0.15	0.08–0.19	26	

NOTES.—Units of right ascension are hours, minutes, and seconds, and units of declination are degrees, arcminutes, and arcseconds. (1) J1888.16 cluster $z = 0.563$. (2) A122 $z = 0.11278$. (3) Abell S154. (4) APMBGC 244−064−098 $z = 0.08764$. (5) A227 $z = 0.17625$. (6) A3038. (7) Abell S346 $z = 0.067$. (8) A3259. (9) A744 $z = 0.0756$. (10) 2′ of PDCS 040. (11) A899. (12) J101016.1+543006 group $z = 0.045$. (13) $z = 0.340$ cluster (Schmidt et al. 1998). (14) UGC 06057 group $z = 0.0382$. (15) MS 1157.3+5548 $z = 0.081$. (16) MS 1201.5+2824 $z = 0.167$. (17) MS 1208.7+3928 $z = 0.340$. (18) MS 1308.8+3244 $z = 0.245$. (19) MKW 11 $z = 0.02314$. (20) $z = 0.308$ cluster (McHardy et al. 1998). (21) $z = 0.382$ cluster (McHardy et al. 1998). (22) RX J13406+4018 group $z = 0.171$. (23) A1774 $z = 0.1691$. (24) A1775 $z = 0.0696$. (25) Probably part of A1877 $z = 0.2493$. (26) Image saturated by a nearby star. (27) A1969 $z = 0.29809$. (28) Distant cluster behind the nearby group. (29) MCG + 04−39−010 group. (30) A2220 $z = 0.1106$. (31) TTR95 1646+82 cluster. (32) QSO 1640+400 $z = 1.59$. (33) A2246 $z = 0.225$. (34) Abell S840 $z = 0.0152$. (35) UGC 11780 group. (36) Part of A2465, z from Jones et al. 1995. (37) Part of A2465, z from Jones et al. 1995. (38) Zw2255.5+2041 $z = 0.288$. (39) A4043.

plates. Photometric calibration was performed using our CCD images and will be described in McNamara et al. (1998). BCG magnitudes were measured in a fixed angular aperture of 5″. No *K*-correction was applied. The X-ray luminosity corrected DSS-II magnitudes are plotted versus redshift in Figure 5. The *m-z* relation can be fit by the relation $m = m_0 + 5 \log z - 1.086(q' - 1)z$ with best-fit parameters $m_0 = 19.84$, $q' = -1.23$. Photometric redshifts were estimated using a procedure analogous to that for the CCD data. The comparison of the estimated and measured redshifts yields the accuracy of the photometric estimate of $\Delta z \approx \pm 0.07$.

6. THE CATALOG

Our cluster catalog is presented in Table 3. The object number is given in column (1). The coordinates (J2000.0) of
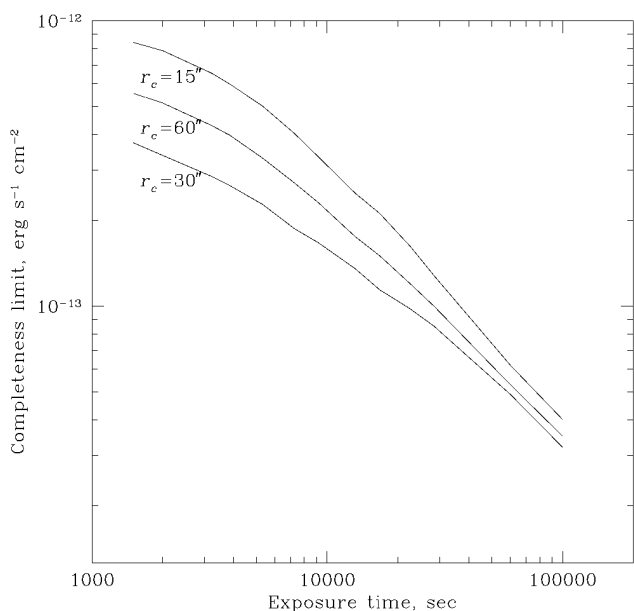

FIG. 6.—Approximate limiting flux, at which the cluster detection probability is 90% in the range of off-axis angles 2′–17.5, plotted vs. exposure time. Limiting fluxes for three values of cluster core radius, $r_c = 15″$, 30″, and 60″, are shown. Sensitivity is best for $r_c \approx 30″$ and declines for smaller and larger clusters.

the X-ray centroid are listed in columns (2) and (3). The total unabsorbed X-ray flux in the 0.5–2 keV energy band (observer frame) in units of ergs s^{-1} cm^{-2} and its uncertainty are listed in columns (4) and (5). The angular core radius and its uncertainty are given in columns (6) and (7). Column (8) contains heliocentric spectroscopic or photometric redshifts. The 90% confidence interval of the photometric redshift is given in column (9). Seven clusters for which the DSS was used for photometric redshift are marked by superscript in column (9). If redshift is spectroscopic, no error interval is given. Three clusters show clear concentrations of galaxies near the X-ray position, but the choice of BCG is uncertain because of the large cluster angular size. We do not list photometric redshifts for these clusters and indicate them by "U" in the "Notes" column. Column (10) lists 90% X-ray position error circle. Column (11) contains notes for individual clusters. In this column, we list the optical identifications from the literature. We also mark likely false detections "F."

Table 4 shows coordinates and exposures for the 647 analyzed *ROSAT* pointings. For a quick estimate of sensitivity in each field, one can use the listed exposure time and Figure 6. In this figure, we show the limiting flux, at which clusters are detected with a probability of 90% for off-axis angles between 2′ and 17.5.

7. MONTE CARLO SIMULATIONS OF CLUSTER DETECTION

For a statistical analysis of our cluster catalog, the detection efficiency as a function of flux and extent and the measurement uncertainty are required. To derive these functions, we used extensive Monte Carlo simulations described in this section.

7.1. *Correcting for Selection Effects*

The most direct way to compare theoretical models with our cluster catalog is to predict the number of clusters within some interval of measured fluxes and radii (and redshift) and then compare the prediction with the number of detected clusters in this interval. To predict the number of detected clusters, one needs to know the detection probability as a function of real cluster flux, f, and radius, r_c, and the distribution of measured values, f_m and $r_{c,m}$, also as a function of f and r_c. Using a theoretical model, one calcu-

TABLE 4

LIST OF *ROSAT* POINTINGS

α	δ	T_{exp} (ks)
00 00 08	+29 57.1	3.5
00 03 22	−26 03.5	38.2
00 05 20	+05 23.9	7.4
00 05 23	−37 21.7	4.7
00 08 18	+20 41.3	23.1
00 10 09	−04 42.1	4.6
00 10 30	+10 58.1	16.8
00 11 23	−11 28.9	6.3
00 18 20	+30 57.7	3.4
00 19 51	+21 57.1	10.5
00 22 08	−15 05.5	9.0
00 22 52	−12 12.7	5.2
00 25 01	−45 29.9	4.6
00 26 18	−42 18.5	8.3
00 27 40	+05 03.5	6.1
00 30 04	−28 42.5	4.3
00 30 04	+26 17.5	24.0
00 33 52	−27 08.5	3.8
00 34 09	−07 22.1	7.6
00 39 20	+30 51.5	26.2
00 40 32	−23 47.9	5.2
00 44 33	−26 11.5	5.4
00 46 13	+01 04.1	10.2
00 48 47	+31 57.7	21.3
00 50 40	−09 28.9	7.8
00 52 06	−29 05.5	22.7
00 53 20	−33 00.1	3.2
00 53 35	+12 41.5	3.4
00 54 52	+25 25.9	5.9
00 54 59	−28 19.7	19.9
00 57 20	−22 22.9	6.3
00 57 28	−27 38.3	42.6
00 57 47	+30 20.9	22.7
00 57 57	−26 13.1	3.8
00 58 06	−27 38.3	26.7
00 59 52	+31 49.9	4.3
01 02 16	−27 19.7	13.3
01 03 56	−30 09.5	3.3
01 08 35	−10 10.9	8.5
01 09 47	+19 39.5	12.8
01 11 28	−38 04.9	10.1
01 12 59	−01 48.7	4.1
01 13 51	−14 50.9	2.3
01 21 51	−28 21.1	2.8
01 23 45	−58 48.7	6.6
01 24 35	+03 48.1	12.0
01 24 45	+09 18.5	10.2
01 28 21	−43 19.3	8.7
01 33 03	−40 06.7	5.9
01 33 44	−07 01.1	3.5
01 34 16	−42 58.3	5.2
01 34 57	−40 56.3	7.2
01 36 25	+20 57.5	8.9
01 36 44	−18 22.1	24.4
01 37 39	−24 30.7	5.4
01 39 40	+17 53.3	16.1
01 39 54	+06 19.1	6.2
01 39 59	+01 31.7	14.4
01 42 32	+20 16.7	3.3
01 43 23	+04 19.9	5.4
01 43 59	+02 20.9	8.7
01 46 39	−00 40.3	4.6
01 48 21	−27 58.1	5.6
01 53 59	−59 47.9	4.2
01 59 51	+00 23.3	5.4
02 03 49	+29 59.5	9.1
02 06 16	−00 17.5	6.3
02 06 21	−12 57.5	3.9
02 06 52	+15 17.9	22.4
02 07 51	+02 43.3	12.0
02 09 28	−39 30.5	23.2
02 09 52	−63 18.5	8.4
02 10 45	−51 01.1	3.8

TABLE 4—*Continued*

α	δ	T_{exp} (ks)
02 14 33	−00 46.3	3.3
02 19 23	−02 58.7	8.3
02 28 39	−10 10.9	7.5
02 34 35	−08 48.1	4.4
02 35 06	−04 01.7	9.1
02 36 11	−52 19.3	14.1
02 38 20	−52 11.5	4.8
02 40 08	−23 09.1	7.2
02 42 40	−00 00.7	7.8
02 52 32	−12 46.1	3.6
02 55 11	+00 10.7	10.6
02 59 04	−00 11.5	3.9
03 03 28	−24 10.3	2.2
03 03 40	+00 23.5	3.8
03 14 13	−23 15.5	15.8
03 15 10	−55 13.9	46.7
03 17 59	−66 55.9	6.2
03 18 08	−34 26.3	4.2
03 19 49	−26 27.1	12.1
03 23 15	−49 31.1	5.7
03 25 27	−06 08.5	5.5
03 33 37	−36 08.5	4.4
03 35 28	−25 44.3	5.7
03 37 56	−25 20.9	34.2
03 42 09	−44 54.7	67.5
03 42 11	−44 07.7	58.4
03 43 15	−09 46.3	5.2
03 51 52	−37 03.5	4.7
03 53 47	−10 25.1	7.6
04 05 33	−13 08.3	5.3
04 07 47	−12 12.1	4.4
04 14 16	−12 44.5	9.8
04 17 16	−05 54.1	3.6
04 22 13	−38 44.9	8.1
04 22 39	−13 21.7	5.5
04 26 01	−57 12.1	3.1
04 28 40	−37 56.5	3.4
04 33 59	−08 34.9	6.4
04 37 28	−47 11.3	5.8
04 40 18	−43 33.1	17.4
04 40 56	−16 30.5	17.5
04 41 21	−27 08.3	3.4
04 45 44	−59 15.1	18.1
04 49 23	−43 50.5	5.8
04 52 32	−29 53.5	2.6
04 53 27	−42 13.9	14.3
04 56 09	−21 59.5	7.9
05 00 44	−30 16.7	7.3
05 05 51	−28 35.3	12.6
05 11 37	−45 00.1	16.9
05 19 44	−45 46.7	3.2
05 20 59	−25 21.5	3.4
05 22 58	−36 27.7	4.6
05 29 27	−32 49.3	31.0
05 29 28	−58 54.5	11.6
05 31 37	−46 24.1	31.7
05 34 49	−58 01.9	9.0
07 47 28	+60 55.9	3.8
08 04 32	+65 00.1	6.4
08 10 03	+42 28.3	3.5
08 10 59	+76 03.1	2.5
08 12 28	+62 36.7	4.7
08 13 13	+45 59.3	13.5
08 13 37	+48 13.3	2.5
08 18 27	+56 44.9	5.9
08 19 04	+70 42.7	13.4
08 19 47	+37 31.3	7.3
08 26 52	+26 37.9	13.7
08 27 04	+31 29.9	5.2
08 32 25	+49 13.3	3.5
08 35 20	+19 35.3	8.4
08 36 44	+53 28.9	7.8
08 37 39	+49 52.9	4.6
08 38 22	+48 37.7	3.9

TABLE 4—*Continued*

α	δ	$T_{\exp}$ (ks)
08 38 47	+36 31.3	9.2
08 39 13	+65 01.1	4.3
08 40 49	+13 12.7	4.6
08 41 18	+64 22.7	24.3
08 41 25	+70 53.3	9.4
08 43 39	+50 12.7	7.6
08 44 27	+12 52.9	4.7
08 44 45	+76 53.3	4.1
08 47 15	+37 32.3	4.3
08 47 44	+34 44.9	3.2
08 48 18	+37 40.1	10.0
08 49 13	+44 50.3	63.0
08 49 58	+51 08.5	3.7
08 50 09	+18 26.5	5.9
08 51 40	+16 12.7	2.6
08 53 11	+13 52.7	17.1
08 53 44	+57 48.5	3.6
08 54 47	+20 06.5	9.6
08 55 04	+17 04.9	13.8
08 58 09	+27 51.1	13.8
08 58 42	+14 08.9	19.5
09 05 30	+34 07.9	26.5
09 06 32	+16 46.1	6.0
09 06 52	+33 40.1	49.7
09 09 32	+54 23.9	30.6
09 09 33	+42 53.9	19.9
09 14 25	+52 41.5	1.9
09 15 57	+53 25.3	5.9
09 18 44	+06 16.9	2.6
09 20 57	+44 42.1	2.5
09 21 09	+45 39.1	3.2
09 21 37	+62 15.7	15.9
09 22 13	+74 59.5	11.8
09 22 29	+71 09.5	2.9
09 25 13	+52 17.3	8.2
09 26 02	+12 43.9	7.6
09 27 03	+39 02.5	22.7
09 28 08	+74 46.7	3.5
09 29 57	+05 38.9	3.3
09 34 01	+55 14.3	14.0
09 35 54	+61 20.9	13.7
09 36 21	+49 43.9	6.8
09 37 05	+81 19.9	6.6
09 39 24	+83 15.7	5.3
09 39 54	+35 53.9	6.8
09 40 21	+50 20.9	6.6
09 41 06	+38 53.9	14.6
09 42 51	+26 01.3	3.4
09 43 44	+16 31.1	8.1
09 44 59	+48 00.1	2.6
09 46 32	+47 45.1	3.1
09 46 37	+44 46.9	3.6
09 47 45	+07 25.1	10.4
09 48 01	+47 59.9	3.2
09 49 32	+47 45.1	3.4
09 49 47	+73 14.3	8.2
09 49 47	+11 06.7	5.6
09 50 49	+39 27.1	11.5
09 50 59	+47 59.9	3.0
09 52 20	−01 36.7	7.1
09 52 32	+46 44.9	1.8
09 53 11	+07 55.9	6.7
09 53 56	−05 04.1	6.8
09 54 01	+47 59.9	3.4
09 54 09	+49 15.7	2.7
09 54 59	−01 30.1	3.1
09 55 32	+47 44.9	2.2
09 56 52	+41 15.5	4.9
09 56 59	+47 30.1	1.6
09 57 39	+55 22.7	3.4
09 58 20	+47 25.1	2.8
09 58 32	+47 44.9	3.0
09 58 32	+46 45.1	4.9
09 58 47	+65 34.1	4.7

TABLE 4—*Continued*

α	δ	$T_{\exp}$ (ks)
10 00 01	+46 30.1	2.5
10 01 40	+17 24.5	5.9
10 01 57	+55 40.9	10.2
10 01 59	−08 09.5	13.0
10 04 20	+05 13.1	7.2
10 06 16	+34 51.7	10.7
10 10 13	+50 44.9	13.5
10 10 13	+52 45.1	12.4
10 10 15	+51 44.9	21.2
10 10 18	+53 45.1	15.1
10 10 18	+54 45.1	14.4
10 10 18	+55 45.1	14.9
10 13 28	+06 11.9	3.5
10 15 04	+49 25.9	4.8
10 18 15	+71 55.7	5.5
10 19 16	+52 44.9	11.8
10 19 37	+19 52.1	22.5
10 24 33	+47 08.9	11.3
10 25 56	+33 47.9	3.0
10 27 14	+53 29.3	13.5
10 31 20	+50 53.3	7.9
10 33 51	+23 08.9	5.2
10 33 52	+58 46.9	3.3
10 34 40	+39 38.5	3.4
10 35 10	+57 04.9	3.1
10 36 23	+03 43.1	3.4
10 37 04	−00 08.5	25.2
10 42 47	+12 03.5	8.4
10 43 11	+74 30.5	3.6
10 44 23	+80 54.5	4.7
10 45 23	+45 34.3	10.2
10 47 11	+63 35.5	4.1
10 47 13	+54 18.7	10.6
10 48 13	−11 20.5	5.0
10 51 37	+54 04.7	10.8
10 51 44	+33 59.3	5.6
10 52 02	+61 25.1	13.4
10 52 04	+57 22.3	128.3
10 53 21	−00 16.7	3.2
10 56 59	+49 41.3	7.9
10 58 28	+01 34.1	4.0
10 59 01	+51 25.9	1.8
11 00 11	−14 04.9	7.7
11 00 51	+39 12.7	8.1
11 02 38	+21 58.3	4.6
11 02 40	+25 04.9	36.5
11 02 54	+60 53.3	15.8
11 03 59	−18 00.1	13.0
11 08 04	+44 51.7	1.8
11 08 11	+44 57.5	12.5
11 10 39	+48 31.1	2.0
11 13 11	−26 28.1	10.0
11 14 08	+20 31.3	17.7
11 14 39	+40 37.1	13.5
11 17 08	+44 13.7	4.9
11 17 16	+17 57.7	7.0
11 18 18	+07 46.1	13.2
11 18 32	+40 25.7	5.4
11 19 09	+21 19.1	32.2
11 20 44	+23 28.1	4.4
11 22 20	+59 04.7	7.2
11 24 16	+14 13.7	6.1
11 24 37	+42 00.7	4.1
11 24 44	+38 45.5	6.3
11 24 44	−17 05.3	4.6
11 25 37	+54 22.9	7.7
11 28 32	+58 33.7	7.8
11 29 16	−04 23.9	15.6
11 36 23	+70 08.3	2.2
11 36 32	+21 36.1	10.5
11 36 35	+29 48.1	26.6
11 38 27	+03 22.3	3.7
11 39 11	+33 01.3	10.4
11 41 16	+21 57.7	1.7

TABLE 4—*Continued*

α	δ	$T_{\rm exp}$ (ks)
11 43 39	+71 41.3	3.0
11 45 08	+72 20.9	11.2
11 46 35	+00 12.7	5.7
11 46 37	−07 40.1	3.7
11 46 51	+28 44.3	13.1
11 49 32	+24 38.9	4.1
11 50 18	+24 17.9	9.7
11 50 39	+01 46.3	5.5
11 53 11	+80 58.1	18.5
11 53 25	+49 31.1	5.2
11 53 40	+46 12.5	3.5
11 53 51	+53 41.3	2.9
11 56 28	+55 07.3	1.6
11 57 57	+55 27.3	38.6
12 01 13	−03 40.7	12.7
12 04 27	−03 40.4	29.1
12 04 42	+27 53.9	18.9
12 05 23	−07 42.5	8.7
12 10 32	+39 24.7	10.9
12 10 57	+09 54.7	5.0
12 12 32	+15 07.1	3.8
12 13 45	+02 48.5	4.8
12 14 16	+14 02.9	7.0
12 16 35	+26 29.3	2.3
12 17 51	+30 07.1	20.4
12 18 25	+30 02.5	14.4
12 18 28	+29 48.5	5.1
12 19 20	+06 38.3	3.1
12 19 25	+05 49.3	11.3
12 20 33	+33 43.3	16.9
12 20 40	+69 05.5	4.1
12 21 04	+49 26.9	2.8
12 21 23	+30 10.7	10.2
12 21 32	+28 13.7	12.5
12 21 44	+75 18.5	20.1
12 22 21	+04 13.1	7.3
12 24 25	+24 36.7	3.4
12 25 37	+24 58.7	6.4
12 25 57	+47 32.9	2.1
12 27 42	+01 36.1	23.0
12 28 25	+31 28.7	7.6
12 29 33	+13 46.1	4.7
12 30 06	+69 11.9	13.9
12 31 32	+64 14.3	1.9
12 32 03	+20 09.7	9.7
12 33 40	+31 01.1	2.6
12 34 56	+37 37.7	7.8
12 36 25	+00 54.5	19.1
12 37 37	+26 43.3	7.2
12 37 44	+11 49.3	7.1
12 41 51	−14 55.9	2.6
12 42 52	+13 15.5	5.2
12 46 35	+02 22.3	3.6
12 46 40	+11 13.1	2.9
12 49 15	−05 59.5	10.5
12 51 15	+25 39.5	13.1
12 52 25	−29 15.1	11.7
12 55 33	+25 53.3	11.7
12 56 13	−05 47.3	76.4
12 56 13	+56 52.1	18.9
12 56 57	+47 20.5	39.9
12 58 09	+35 19.7	2.5
13 00 01	+12 40.1	5.7
13 00 49	+12 22.7	3.5
13 02 09	+10 57.5	3.5
13 05 33	−10 33.7	3.1
13 05 44	+18 01.1	3.3
13 09 49	+08 19.9	7.0
13 10 30	+32 20.9	7.6
13 10 57	+37 03.7	7.3
13 11 35	−05 52.9	11.0
13 11 52	+27 52.7	5.7
13 12 16	+35 15.5	2.8
13 20 20	+69 01.1	2.1

TABLE 4—*Continued*

α	δ	$T_{\rm exp}$ (ks)
13 21 03	+01 53.5	3.6
13 22 51	+54 55.1	3.7
13 23 40	−01 27.7	4.8
13 23 51	+65 41.9	6.0
13 25 15	+54 59.5	3.1
13 25 44	−29 49.9	9.0
13 28 23	+13 46.9	3.0
13 28 28	+11 44.5	4.6
13 29 09	+29 50.5	6.2
13 29 47	+01 05.9	7.7
13 30 49	+24 13.7	3.9
13 32 25	+11 06.5	9.1
13 32 52	+02 00.7	7.2
13 34 35	+37 54.5	88.5
13 34 45	−08 20.5	10.0
13 35 27	+38 12.1	5.6
13 35 49	+38 20.9	5.3
13 36 16	+38 29.9	6.8
13 36 40	+51 54.5	3.2
13 36 42	+38 38.3	6.2
13 37 06	+38 47.3	6.9
13 37 21	+24 22.9	2.7
13 37 30	+38 55.7	4.3
13 37 35	+26 37.9	7.7
13 37 37	+27 31.9	8.4
13 37 40	−12 57.5	2.3
13 37 54	+39 04.7	4.4
13 38 16	+48 16.7	9.2
13 38 18	+39 13.7	5.5
13 38 45	+39 22.1	4.9
13 39 09	+39 31.1	5.3
13 39 30	+27 49.1	7.5
13 39 33	+27 04.7	5.5
13 39 35	+39 39.7	6.2
13 39 35	+26 21.1	8.6
13 40 01	+39 48.7	5.7
13 40 25	+39 57.7	5.1
13 40 49	+40 06.1	5.8
13 41 03	+51 53.9	13.2
13 41 15	+40 15.1	5.3
13 41 28	+27 31.9	9.4
13 41 32	+26 37.9	7.7
13 41 37	+40 23.9	6.0
13 42 01	+40 32.3	7.4
13 42 08	+35 39.1	4.7
13 42 28	+40 41.5	5.7
13 42 51	+27 04.7	9.0
13 42 54	+40 49.7	5.3
13 43 16	+40 58.7	6.1
13 43 42	+00 15.1	19.7
13 44 44	+55 53.3	28.1
13 47 33	+12 17.3	3.1
13 48 54	+07 57.5	23.6
13 53 02	+69 18.5	7.6
13 53 16	+63 45.7	7.6
13 54 08	−02 05.9	14.3
13 54 08	−01 59.9	9.9
13 54 35	+18 05.5	5.3
13 56 01	+18 22.3	18.3
13 56 09	+25 55.1	12.1
14 00 32	+04 04.9	3.8
14 04 09	+09 37.9	7.4
14 04 38	+43 27.7	5.3
14 04 51	+04 01.7	4.5
14 05 16	+25 55.9	3.4
14 06 04	−07 58.1	2.9
14 06 23	+22 23.9	6.7
14 06 42	+34 11.3	20.6
14 06 59	+28 26.9	24.5
14 08 32	+59 40.9	2.5
14 09 23	+26 18.7	3.1
14 13 15	−03 12.7	2.6
14 13 47	+43 59.9	22.5
14 15 42	+19 11.5	15.4

TABLE 4—*Continued*

TABLE 4—*Continued*

α	δ	$T_{\rm exp}$ (ks)
14 15 45	+11 29.8	25.4
14 15 57	+13 20.3	2.1
14 16 01	−05 59.5	2.7
14 17 01	+44 56.5	6.3
14 17 21	+26 51.7	5.4
14 17 56	+25 43.3	2.6
14 17 59	+25 08.5	40.9
14 19 06	+06 28.9	15.9
14 19 16	+13 00.1	3.3
14 19 45	+54 23.3	9.8
14 22 56	+32 50.9	6.6
14 26 59	+23 47.5	2.8
14 27 35	+26 32.5	6.5
14 28 32	+42 40.3	6.4
14 28 42	+33 10.9	28.5
14 29 06	+01 17.3	5.4
14 29 42	+47 47.3	5.9
14 36 21	+58 47.5	3.5
14 38 59	+64 17.3	14.2
14 43 03	+52 01.9	6.2
14 44 35	+63 36.5	3.2
14 44 52	+29 19.1	3.8
14 45 16	+09 58.7	12.4
14 46 46	+40 34.9	4.5
14 57 46	+40 43.7	5.6
14 59 08	+71 40.3	7.6
14 59 59	+65 35.9	2.1
15 01 03	+22 37.9	4.3
15 01 57	+40 23.3	9.9
15 02 08	+66 12.7	2.9
15 04 01	+10 26.5	15.2
15 11 01	+66 20.9	2.0
15 11 51	+61 51.5	2.9
15 13 35	+38 34.1	8.2
15 14 44	+36 51.1	4.7
15 14 47	+44 01.9	7.6
15 18 11	+31 39.1	17.4
15 21 15	+22 27.5	3.8
15 22 56	+66 04.9	3.5
15 24 25	+09 58.3	8.0
15 24 28	+30 32.3	3.4
15 24 56	+58 58.1	5.4
15 26 08	+41 40.3	7.4
15 26 58	+35 58.9	3.6
15 27 03	+42 04.1	5.0
15 33 51	+63 54.5	3.3
15 34 40	+26 43.1	34.9
15 35 10	+03 11.5	3.1
15 35 52	+57 53.9	5.1
15 37 09	+11 55.9	5.0
15 40 51	+14 47.9	6.8
15 42 13	+18 35.3	4.8
15 44 01	+53 58.7	5.4
15 44 16	+06 25.7	3.9
15 45 30	+48 46.1	10.3
15 47 44	+20 52.3	2.8
15 49 51	+21 25.9	14.2
15 50 35	+40 25.9	2.0
15 50 44	+11 20.9	3.8
15 51 21	+71 45.1	5.2
15 52 09	+20 06.1	13.5
15 52 39	+42 26.3	3.6
15 52 47	+18 56.5	2.1
15 54 23	+20 12.1	3.5
15 59 11	+35 01.7	6.1
16 05 47	+25 51.5	22.7
16 06 06	+23 36.7	9.4
16 13 59	+65 43.1	6.9
16 17 08	+55 16.1	4.8
16 17 44	+32 22.3	9.0
16 17 47	+06 04.1	8.5
16 19 44	+46 18.5	3.5
16 20 13	+17 24.7	5.1
16 20 21	+17 36.5	7.3

α	δ	$T_{\rm exp}$ (ks)
16 23 59	+61 30.5	7.6
16 25 21	+54 18.7	4.8
16 29 03	+40 07.9	4.0
16 29 52	+24 26.5	3.1
16 30 13	+21 29.3	4.6
16 30 18	+37 19.3	7.5
16 32 32	+82 32.3	12.6
16 33 04	+41 57.7	11.3
16 33 23	+47 19.1	2.9
16 34 25	+57 09.1	37.3
16 34 28	+70 31.9	8.3
16 34 33	+62 45.7	3.8
16 35 15	+38 07.7	4.4
16 38 27	+34 59.9	3.2
16 40 57	+53 41.5	20.6
16 41 16	+39 54.1	2.1
16 42 52	+38 55.3	4.4
16 42 58	+39 48.5	10.5
16 43 49	+17 15.5	14.3
16 53 52	+39 45.5	5.5
16 58 50	+34 18.7	5.2
16 59 51	+44 01.1	4.6
17 00 44	+57 12.5	3.7
17 01 01	+64 11.9	32.8
17 01 25	+51 49.3	6.5
17 04 40	+60 44.3	23.2
17 06 35	+23 58.3	6.9
17 07 01	+53 11.9	16.4
17 08 44	+71 07.7	26.9
17 12 56	+33 31.3	13.5
17 15 03	+36 48.5	6.6
17 15 03	+44 29.9	4.5
17 17 08	+43 08.3	5.9
17 19 37	+48 04.3	11.0
17 19 58	+57 49.9	3.6
17 24 04	+41 14.3	3.2
17 26 11	+74 31.1	8.1
17 28 20	+50 13.1	3.6
17 34 20	+38 57.7	5.1
17 46 15	+62 27.1	10.0
17 48 33	+70 05.9	2.2
17 48 38	+68 41.9	19.5
17 54 08	+67 08.5	1.7
17 55 49	+66 08.3	2.9
17 57 56	+66 22.7	25.9
20 04 20	−56 02.9	5.5
20 09 25	−48 49.9	21.7
20 18 52	−57 21.5	3.5
20 37 32	−22 42.7	10.8
20 37 33	−47 17.3	5.1
20 47 45	−36 35.5	61.1
20 54 47	−58 27.1	4.2
20 58 20	−18 14.5	5.4
21 00 08	−42 38.9	12.4
21 04 11	−11 22.3	3.5
21 07 56	−05 16.1	19.6
21 09 20	−13 14.3	16.7
21 14 23	−67 47.3	21.4
21 17 30	−38 51.1	13.7
21 23 01	−16 10.9	5.1
21 29 11	−15 38.9	9.1
21 31 33	−05 34.3	6.8
21 34 09	−01 53.3	5.5
21 36 39	+00 42.1	5.1
21 40 15	−43 10.1	7.5
21 40 20	−23 10.7	3.7
21 45 52	+07 17.9	2.2
21 46 35	+04 13.9	22.0
21 49 35	−43 06.7	8.5
21 56 21	+07 22.3	6.7
21 58 08	−15 01.1	8.6
22 00 35	−02 44.3	5.1
22 02 25	−41 15.1	9.1
22 02 59	−56 45.1	13.2

TABLE 4—*Continued*

α	δ	T_{exp} (ks)
22 03 04	−18 55.1	12.1
22 05 47	+00 19.3	4.3
22 09 06	−27 48.5	12.6
22 09 20	−47 10.3	4.4
22 12 59	−17 10.1	9.5
22 13 59	+12 41.9	3.5
22 14 11	−49 19.1	3.6
22 15 16	−29 59.3	7.5
22 17 11	+14 14.5	6.9
22 23 45	−02 13.1	9.3
22 25 39	+21 18.1	6.3
22 25 49	−04 56.9	14.2
22 30 40	−39 42.7	3.5
22 34 09	+00 00.1	2.7
22 35 45	−26 03.1	19.7
22 36 08	+13 43.7	5.3
22 39 52	−05 52.3	8.1
22 43 27	−25 44.5	3.5
22 45 20	−46 52.1	5.3
22 46 57	+03 24.5	4.0
22 48 40	−51 10.1	4.3
22 49 40	−27 06.7	8.6
22 50 23	+14 19.9	6.7
22 51 51	−17 52.1	4.0
22 54 46	−37 23.5	5.1
22 55 16	−03 10.7	6.8
22 57 30	+20 46.3	9.3
22 57 40	−36 56.5	8.3
23 01 52	−55 08.5	8.2
23 03 15	+08 52.9	19.5
23 04 35	−51 28.1	13.9
23 04 39	−35 01.1	8.7
23 04 44	−08 41.3	28.4
23 05 23	−35 52.1	9.1
23 08 40	−27 25.7	8.2
23 13 59	−49 39.7	18.1
23 16 03	−05 27.1	13.6
23 16 55	+25 43.0	2.1
23 18 21	−42 22.3	6.8
23 18 47	+12 36.1	8.9
23 18 56	−00 14.3	5.2
23 20 32	+17 13.9	10.3
23 25 01	−54 41.9	3.8
23 25 23	+23 24.1	22.0
23 28 35	+14 45.1	8.2
23 31 37	−01 48.1	4.0
23 32 57	−37 49.3	7.6
23 36 21	+02 09.5	9.1
23 43 32	−14 55.3	11.1
23 49 25	−31 25.7	6.2
23 50 09	−26 22.9	3.0
23 51 21	+20 06.5	9.2
23 51 56	+28 55.1	5.3
23 51 56	−01 09.1	6.3
23 54 32	−15 13.1	4.6
23 55 03	+28 37.9	3.4

NOTE.—Units of right ascension are hours, minutes, and seconds, and units of declination are degrees and arcminutes.

lates the number of real clusters as a function of flux and radius, then multiplies this number by the detection probability, and then convolves it with the measurement scatter.

Since the detection algorithm for extended sources is rather complicated, the only method of deriving appropriate corrections is through Monte Carlo simulations.

7.2. *What Affects the Cluster Detection?*

In this section, we discuss the effects that influence the cluster detection process, and which therefore should be included in Monte Carlo simulations.

The first obvious effect is the degradation of the *ROSAT* angular resolution at large off-axis angles. Because of this degradation, a cluster with $r_c = 20''$ is well resolved on-axis where the FWHM of the PSF is 25″, but the same cluster is indistinguishable from a point source if located at an off-axis angle of 17′ where the PSF is 57″ (FWHM).

Point sources, which may lie in the vicinity of a cluster, reduce the efficiency of cluster detection and increase the measurement errors. Therefore, the simulations should include realistic spatial and flux distributions of point sources.

In addition, exposure time, Galactic absorption, and the average background level vary strongly among the analyzed *ROSAT* fields, and so does the probability to detect a cluster of given flux. Also, the background has to be modeled individually for each field and cannot be assumed known in simulations.

To model all these effects, we simulate realistic *ROSAT* images containing point sources, insert clusters with known input parameters at random positions into the simulated images, and analyze these images identically to the real data. The selection functions are then derived from comparison of the numbers and parameters of input and detected clusters.

7.3. *Simulating ROSAT Images without Clusters*

We begin with point sources that are the major contributor to the X-ray background in the *ROSAT* band. To simulate source fluxes, we use the log N–log S relation measured in the flux range of 1.2×10^{-15} to 10^{-12} ergs s^{-1} cm^{-2} (Vikhlinin et al. 1995b). Fluxes are simulated using the extrapolation of log N–log S in the range from 10^{-11} to 2.5×10^{-17} ergs s^{-1} cm^{-2}, where the integral emission of point sources saturates the X-ray background. Source positions are simulated either randomly or with a nonzero angular correlation function using a two-dimensional version of the Soneira & Peebles (1978) algorithm. After the source position is determined, we convert the flux to the number of detected photons using the exposure time at the source position and the counts-to-flux conversion appropriate to a power-law spectrum with $\Gamma = 2$ and the actual Galactic absorption in the simulated field. The number of detected source photons is drawn from a Poisson distribution. The photon positions are simulated around the source position according to the PSF as a function of off-axis angle. Finally, we add a flat Poisson background (corrected for the exposure variations across the field) until the average background levels are equal in the simulated image and the corresponding real observation. This flat uniform component corresponds to truly diffuse backgrounds, such as foreground Galactic emission, scattered solar X-rays, and the particle background.

The images simulated according to the described procedure correctly reproduce fluxes and the spatial distribution of point sources, the average background level, and background fluctuations caused by undetected point sources and their possible angular correlation.

7.4. *Simulations of Clusters*

The next step is to put a cluster of a given flux and angular size at a random position in the image. An elliptical

β-model,

$$I(x, y) = I_0(1 + x^2/a_x^2 + y^2/a_y^2)^{-3\beta + 1/2} , \qquad (4)$$

was used for cluster brightness. Cluster β parameters and axial ratios were randomly selected from the distribution observed in nearby clusters (Jones & Forman 1998; Mohr et al. 1995). To include the influence of edge effects arising because detected clusters must lie between off-axis angles of $2'$ and 17.5, cluster positions were simulated in the inner 18.5 circle of the field of view. Cluster flux was converted to the number of detected photons using the local exposure and the counts-to-flux coefficient corresponding to a $T = 5$ keV plasma spectrum and the Galactic absorption for the field. The cluster model was convolved with the PSF calculated for the given off-axis angle. Photons were simulated using a Poisson distribution around the model and added to the image.

Reducing simulated images identically to the real data, we derive the detection efficiency as a function of flux and effective radius. Effective radius is defined as the radius at which the radially averaged surface brightness drops by a factor of $2^{3/2}$ (§ 4.2). The effective radius can be calculated from parameters in equation (4) as

$$r_e = \sqrt{a_x a_y (2^{1.5/(3\beta - 0.5)} - 1)} . \qquad (5)$$

In simulations, we verified that the detection probability indeed has very little dependence on the β-parameter and axial ratio and is determined by r_e only.

7.5. *Simulation Runs*

Simulated images were reduced identically to the real data, i.e., we modeled the background (§ 2), detected candidate extended sources by the wavelet decomposition (§ 3.2), fitted these candidate sources and applied our final selection criteria (§ 3.3), and recorded parameters of input and detected clusters. Each of the 647 *ROSAT* fields was simulated 650 times. Radii and fluxes of input clusters were randomly distributed in the $5''$–$300''$, 10^{-14} to 3×10^{-12} ergs s^{-1} cm^{-2} range.

To derive the distribution of false detections, we performed a separate set of simulations without putting clusters into simulated images. In this set of simulations, each field was simulated 50 times.

Simulations were performed with point sources distributed either randomly or with the angular correlation function measured by Vikhlinin & Forman (1995) for faint *ROSAT* sources. The spatial correlation of point sources significantly increases the number of false detections (by a factor of 1.5) but has little or no effect on the detection probability of real clusters.

The simulation results were used to measure the cluster selection functions necessary for a statistical study of our catalog.[4]

7.6. *Results of Simulations: Detection Probability*

The probability that a cluster with unabsorbed flux f and radius r_e, whose position falls within 18.5 of the center of one of the analyzed *ROSAT* fields, will be detected is shown in Figure 7. This probability is normalized to the geometric

---

[4] These data are available in electronic publication on AAS CD-ROM and through the WWW page http://hea-www.harvard.edu/x-ray-clusters/.
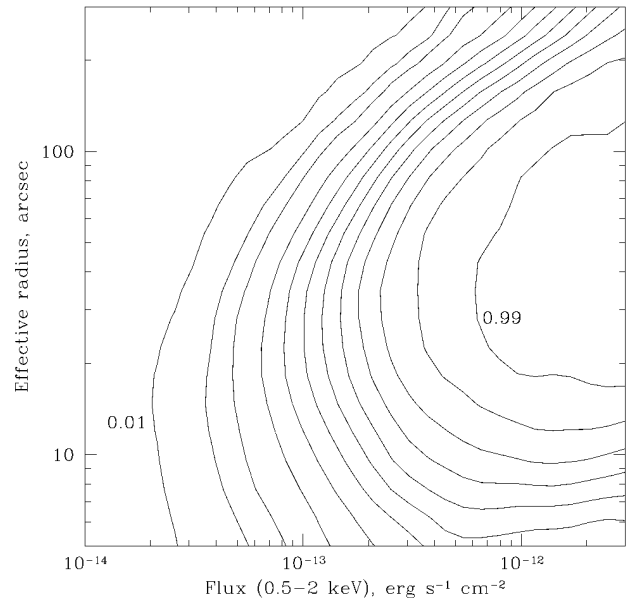
FIG. 7.—Probability of cluster detection as a function of flux and core radius. Contours correspond to the detection probabilities of 1%, 5%, 10%, 20%, 30%, 40%, 50%, 60%, 70%, 80%, 90%, and 99%.

area of the annulus in which detected clusters may be located ($2'$–17.5). At a given flux, the detection probability is the highest for clusters with radii of $\sim 30''$. It gradually decreases for clusters with large radius because their flux is distributed over the larger area, thus decreasing their statistical significance. The detection probability also decreases for compact clusters because they become unresolved at large off-axis angles. This effect is important for clusters with angular core radii of $\lesssim 15''$. Even at $z = 1$ this radius corresponds to 130 kpc, which is 2 times smaller than the core-radius of a typical rich cluster (250 kpc; Jones & Forman 1998). Therefore, cluster detection efficiency is limited mainly by the low number of photons, not by the resolution of the *ROSAT* PSPC.

The detection probability changes by less than 10% for clusters with axial ratios < 0.7 compared to azimuthally symmetric clusters. This is caused by significant PSF smearing, which reduces the apparent ellipticity of distant clusters. Similarly, we have found no significant dependence of the detection probability on the value of the β-parameter.

7.7. *Results of Simulations: Measurement Scatter and Bias*

In this section, we consider the distributions of measured flux and radius of detected clusters, as functions of input flux and radius. These distributions are derived for clusters detected in *any* field and at *any* off-axis angle and is different from the errors listed in Table 3, which are determined only by the photon counting statistics. Figure 8 shows the distributions derived for several values of input cluster flux and radius. The points in this figure represent the mean relative deviation of the observed parameter, while the error bars show the mean relative scatter (both positive and negative). Generally, the flux measurement is unbiased and has a small relative scatter of $\sim 20\%$. At low fluxes, at which the detection probability decreases, the measured fluxes tend to be overestimated. This bias is naturally present whenever a flux measurement is performed near the detection threshold and is not related to the particular detection algorithm. For example, a source with a true flux exactly equal to the detec-
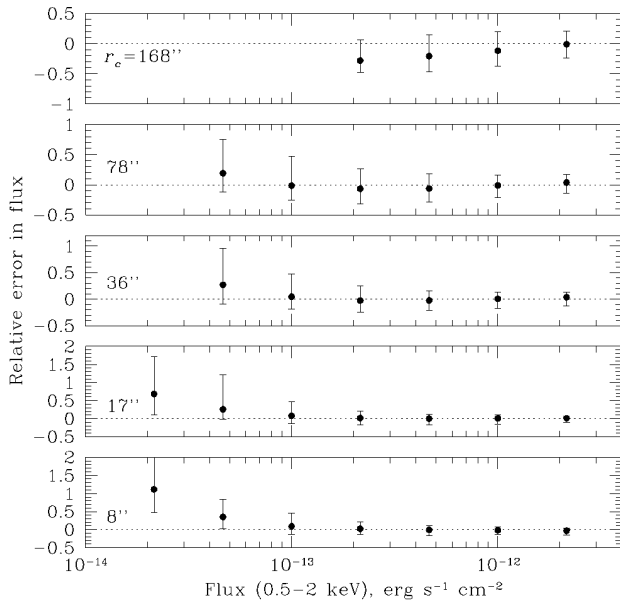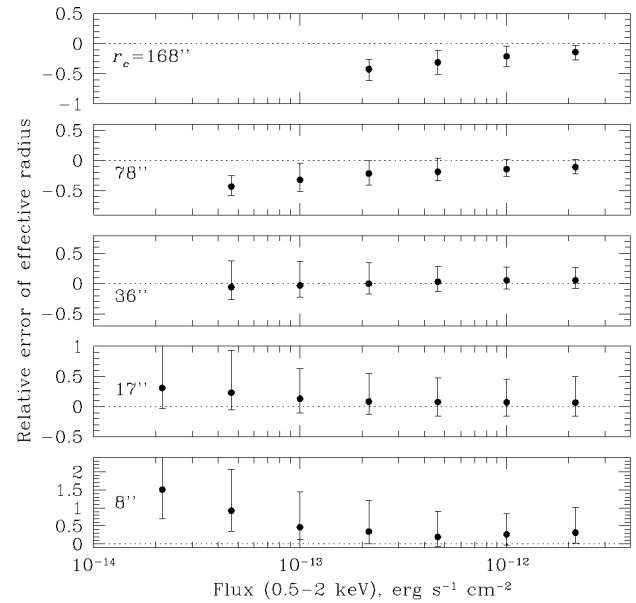
FIG. 8a

FIG. 8b

FIG. 8.—Bias and scatter of flux and radius measurements. Points show the average relative deviation of the measured quantity. Error bars show the relative scatter of the measured quantity, not errors of bias.

tion threshold will be detected with 50% probability, and in all these cases the measured flux exceeds the true flux. Averaged over detections, the measured flux exceeds the true value. This flux bias should be accounted for in deriving the luminosity functions and the log N–log S relation. On the other hand, for clusters with very large radii, the flux is underestimated because the background is overestimated near broad clusters. This effect is important only for clusters at low redshifts, which have large angular core radii.

The radii of very compact clusters are strongly overestimated on average because such clusters can be detected as extended sources only if their measured radius is a positive fluctuation with respect to the true value, similar to the flux bias above. The measured radii of very broad clusters are underestimated because of the oversubtraction of the background. The sizes of distant clusters mostly fall in the range of 15″–1′, at which our radius measurements are unbiased. For example, a radius of 250 kpc corresponds to 45″ at $z = 0.3$, 35″ at $z = 0.5$, and 29″ at $z = 1$. At $z < 0.2$, 250 kpc corresponds to large angular radii, and therefore measured sizes of large low-redshift clusters are underestimated.

7.8. Results of Simulation: False Detections

Because of the finite angular resolution of the ROSAT PSPC, closely located point sources can be falsely classified as a single extended source. Optical identification is the most direct way of finding such false detections. However, optical observations alone, with no estimate of the number of false detections, could result in our failure to identify interesting new classes of objects such as quasars lensed by "dark" clusters (Hattori et al. 1997), clusters dominated by a single galaxy (Ponman et al. 1994), and "failed" clusters (Tucker et al. 1995). Therefore, it is desirable to have an independent estimate of the number of false detections and their distribution as a function of flux and radius. For this, we simulate ROSAT images without clusters and reduce them identically to the real data. All the extended sources detected in these simulations are false. Since the simulations

correctly reproduce fluxes and spatial distribution of point sources and all the instrumental artifacts of the ROSAT PSPC, the expected number of false detections can be accurately measured.

Confusion of point sources is the main effect leading to false cluster detections. The degree of confusion depends strongly on whether point sources are distributed randomly or have angular correlation, and the number of false detections changes correspondingly. From simulations, we derive that our source catalog should on average contain 17.2 false detections if point sources are randomly located. If point sources have correlation with the observed amplitude (Vikhlinin & Forman 1995), the number of false detections increases to 25.9. Figure 9 shows the distribution of false detections in radius versus flux coordinates and their cumulative distribution as a function of flux, obtained for correlated point sources. For randomly located sources, the distributions in Figure 9 should simply be scaled. The contamination of our extended source catalog by confused point sources is between 8% and 11%.

The predicted number of false detections agrees well with results of optical identifications. From simulations, we expect on average ≈ 1.5 false detections with fluxes $> 2 \times 10^{-13}$ ergs s^{-1} cm^{-2}. Of 82 X-ray sources above this flux, 80 are optically confirmed clusters, and one is a likely false detection. In the total sample, we expect ≈ 17–26 false sources, while 19 false detections are found in the data (Table 2). Finally, the distribution of flux and core radius of X-ray sources without optical cluster counterparts matches well the distribution for false detections found in simulations (Fig. 9). Thus, our sample provides no support for the existence of "dark" clusters.

7.9. Sky Coverage as a Function of Flux

To compute the log N–log S function, the survey solid angle as a function of flux is required. Traditionally, the sky coverage is thought of as the area in which a survey is "complete," i.e., in which all sources above the given flux
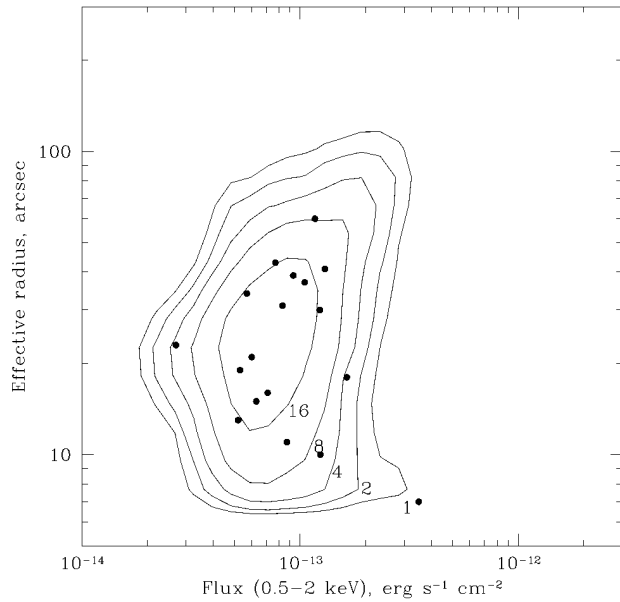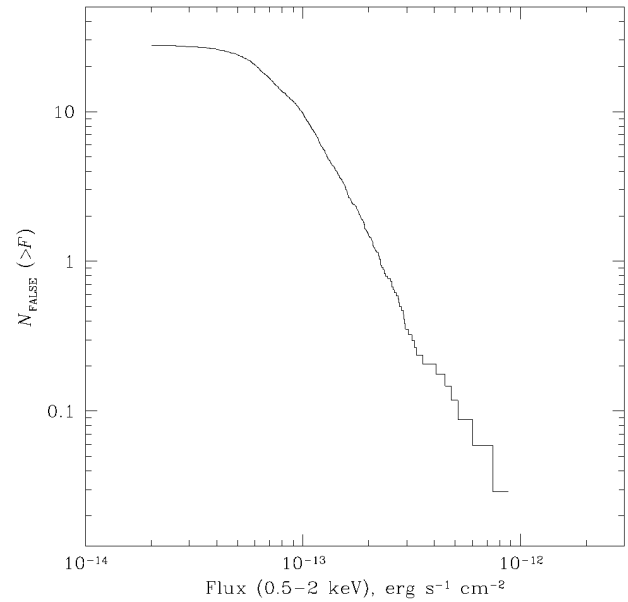
FIG. 9*a*

FIG. 9*b*

FIG. 9.—(*a*) Distribution of false sources as a function of measured flux and radius; (*b*) cumulative distribution as a function of flux. In (*a*), contours represent the levels of equal density of false source distribution. Contour labels show the number of false sources outside the contour. Points represent parameters of the likely false detections in the data, i.e., those X-ray sources that have no cluster counterparts in deep CCD images.

are detected. The differential log N–log S is computed as the ratio of the number of detected sources in a given flux bin and the sky coverage in this flux bin. However, this view of the sky coverage is not correct in the presence of significant flux measurement errors, which is the case in all *ROSAT* surveys. First, the source detection probability changes gradually from 0 to 1 in a flux range of finite width and cannot be adequately approximated by a steplike function of flux. Second, the measurement scatter leads to significant biases in the derived log N–log S relation, as we describe below. Some intrinsically bright sources have low measured fluxes, while some intrinsically faint sources have high measured fluxes. For surveys with uniform sensitivity, the number of sources usually increases at faint fluxes, and the described effect leads to overestimation of log N–log S (Eddington 1940). In X-ray surveys, the sky coverage usually drops rapidly at faint fluxes, and therefore the number of detected sources decreases at faint fluxes. In this case, the sign of the Eddington bias is opposite and the log N–log S function is underestimated (see Fig. 6 in Hasinger et al. 1993b).

For a plausible model of the source population, one can calculate the ratio of the differential log N–log S for detected and real sources if the detection probability and measurement scatter is known. The ratio of these log N–log S functions has the usual meaning of the sky coverage. This approach to the survey area calculation was used by Vikhlinin et al. (1995a, 1995b) to obtain an unbiased measurement of the log N–log S relation for point sources. We use the same approach here to define the survey area for the present cluster survey. We assume nonevolving clusters with the luminosity function of Ebeling et al. (1997) in a $q_0 = 0.5$ cosmology. The distribution of cluster radii and their correlation with luminosities is adopted from Jones & Forman (1998). We simulate cluster redshifts between $z = 0$ and $z = 2$ using the cosmological volume-per-redshift law (see, e.g., Peebles 1993). We then simulate the rest frame

luminosity between $L_X = 10^{42}$ and 10^{46} ergs s^{-1}. Cluster radius is simulated from the distribution corresponding to the simulated luminosity. We then calculate the observed angular radius and flux accounting for the correlation between X-ray luminosity and temperature (David et al. 1993) and the probability to detect this cluster (§ 7.6). Finally we simulate the measured flux (§ 7.7). The detection probability is added to the distribution of detected clusters as a function of measured flux, and 1 is added to the number of input clusters in the corresponding bin of real flux. Simulating 10^6 clusters according to this procedure, we determine the sky coverage as the ratio of detected and input sources in the corresponding flux bins. The calculated survey area is shown in Table 5. In this table we also show the sky coverage for the distant, $z > 0.5$, subsample. The sky coverage for the distant subsample differs from that for the

TABLE 5
SKY COVERAGE OF THE SURVEY

LIMITING FLUX (ergs s^{-1} cm^{-2})	SOLID ANGLE	
	Entire Sample (deg^2)	$z > 0.5$ Clusters (deg^2)
1.3×10^{-14}......	0.074	0.070
1.5×10^{-14}......	0.094	0.089
2.0×10^{-14}......	0.185	0.190
3.0×10^{-14}......	1.354	1.364
4.5×10^{-14}......	9.026	9.100
7.0×10^{-14}......	34.74	34.03
1.0×10^{-13}......	66.55	66.20
1.5×10^{-13}......	102.6	104.3
2.0×10^{-13}......	122.8	127.4
3.0×10^{-13}......	140.9	147.0
4.5×10^{-13}......	148.1	154.0
7.0×10^{-13}......	149.3	159.6
1.0×10^{-12}......	151.1	161.3
1.5×10^{-12}......	157.1	164.7
2.0×10^{-12}......	158.5	165.1

entire sample because of the different distribution of angular sizes.

Using different cluster evolution models (including evolution of luminosities, number density, and radii), we verified that the derived sky coverage varies by no more than 10% compared to the no-evolution assumption, if cluster radii do not evolve. Using the present cluster sample, Vikhlinin et al. (1998) show that the distribution of sizes of distant and nearby clusters is indeed very similar.

8. log N–log S RELATION FOR CLUSTERS

Using the survey solid angle, we calculate the log N–log S relation for clusters. Each optically confirmed cluster is added to the cumulative distribution with the weight equal to the inverse solid angle corresponding to its measured flux. The derived cumulative log N–log S function is shown in Figure 10. We also show the cluster counts derived in other surveys: EMSS (adopted from Jones et al. 1998), the *ROSAT* All-Sky survey sample of X-ray brightest clusters (BCS; Ebeling et al. 1997), the WARPS survey (Jones et al. 1998), Rosati et al. (1995, 1998), and an ultradeep UK *ROSAT* survey (McHardy et al. 1998). The log N–log S relation derived from our survey spans more than 2.5 orders of magnitude in flux. At the bright end, our result shows excellent agreement with the samples of nearby clusters from the BCS and EMSS. At intermediate fluxes, around 2×10^{-13} ergs s^{-1} cm^{-2}, our cluster counts agree well with a small-area WARPS survey. Finally, the extrapolation of our log N–log S relation down to 3×10^{-15} ergs s^{-1} cm^{-2} agrees with results of McHardy et al. (1998), who identified most of the X-ray sources, regardless of extent, in their ultradeep survey. Our log N–log S relation seems to be systematically higher than the surface density of clusters identified in the 50 deg^2 survey of Rosati et al. For example, the difference is a factor of 1.3 at a flux of 2×10^{-13} ergs s^{-1} cm^{-2}, where we optically confirmed 98% of detected sources and where the survey area corrections are relatively small. This difference is marginally significant at the $\sim 2\ \sigma$ level. Since Rosati et al. have not published their cluster sample nor the details of the survey area calculations, it is hard to assess the source of this discrepancy. We only note that it can be explained, for example, if there is a systematic difference of 15%–20% in fluxes. A discrepancy of our log N–log S relation with the EMSS near their sensitivity limit is most likely due to the difference in measured fluxes (§ 4.3).

9. SUMMARY

We present a catalog of 203 clusters detected as extended X-ray sources in 647 *ROSAT* PSPC observations covering a solid angle of 158 deg^2. To detect these sources, we used a novel detection algorithm combining a wavelet decomposition to find candidate extended sources and maximum-likelihood fitting to evaluate the statistical significance of the source extent. Optical identifications demonstrate a high success rate for our X-ray selection: 91% of detected sources in the total sample and 98% in the bright subsample are optically confirmed as clusters of galaxies. We present X-ray parameters of all detected sources and spectroscopic or photometric redshifts for optically confirmed clusters. Extensive Monte Carlo simulations of our source detections are used to derive the sky coverage of the survey necessary for a statistical study of X-ray properties of our clusters. We present the log N–log S relation derived from our cluster catalog. This relation shows a general agreement with other, smaller area surveys.
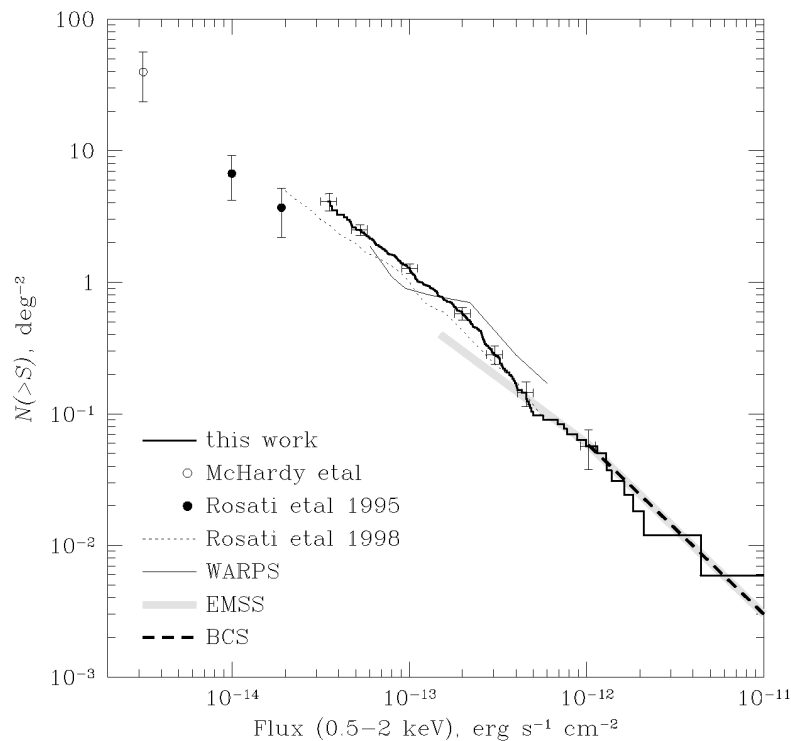

FIG. 10.—Cluster log N–log S relation. The results from our survey are shown as the heavy solid histogram with several individual points including error bars. Vertical error bars represent the uncertainty in the number of clusters, while horizontal error bars correspond to a possible systematic uncertainty in flux (§ 4.3). Other surveys are shown for comparison.

In a subsequent paper (Vikhlinin et al. 1998), we use this sample to constrain the evolution of cluster luminosities and radii at high redshift.

REFERENCES

Birkinshaw, M., Hughes, J. P., & Arnaud, K. A. 1991, ApJ, 379, 466
Briel, U. G., et al. 1996, *ROSAT* User's Handbook (MPE calibration memo)
Burstein, D., & Heiles, C. 1982, AJ, 87, 1165
Cash, W. 1979, ApJ, 228, 939
Castander, F. J., et al. 1995, Nature, 377, 39
Cavaliere, A., & Fusco-Femiano, R. 1976, A&A, 49, 137
Collins, C. A., Burke, D. J., Romer, A. K., Sharples, R. M., & Nichol, R. C. 1997, ApJ, 479, L117
Damiani, F., Maggio, A., Micela, G., & Sciortino, S. 1997, ApJ, 484, 350
David, L. P., Slyz, A., Jones, C., Forman, W., Vrtilek, S. D., & Arnaud, K. A. 1993, ApJ, 412, 479
Dickinson, M. 1996, preprint (astro-ph 9612177)
Ebeling, H., Edge, A. C., Fabian, A. C., Allen, S. W., Craford, C. S., & Böhringer, H. 1997, ApJ, 479, L101
Eddington, A. S. 1940, MNRAS, 100, 354
Edge, A. C., Stewart, G. C., & Fabian, A. C. 1992, MNRAS, 258, 177
Fabian, A. C. 1994, ARA&A, 32, 277
Gioia, I. M., Maccacaro, T., Schild, R. E., Wolter, A., Stocke, J. T., Morris, S. L., & Henry, J. P. 1990, ApJS, 72, 567
Grebenev, S. A., Forman, W., Jones, C., & Murray, S. 1995, ApJ, 445, 607
Hasinger, G., Boese, G., Predehl, P., Turner, T., Yusaf, R., George, I., & Rohrbach, G. 1993a, GSFC OGIP Calibration Memo CAL/ROS/93-015
Hasinger, G., Burg, R., Giacconi, R., Schmidt, M., Trümper, J., & Zamorani, G. 1993b, A&A, 275, 1
Hattori, M., et al. 1997, Nature, 388, 146
Henry, J. P. 1997, ApJ, 489, L1
Henry, J. P., & Arnaud, K. A. 1991, ApJ, 372, 410
Henry, J. P., Gioia, I. M., Maccacaro, T., Morris, S. L., Stocke, J. T., & Wolter, A. 1992, ApJ, 386, 408
Högbom, J. A. 1974, A&AS, 15, 417
Hudson, M. J., & Ebeling, H. 1997, ApJ, 479, 621
Jones, C. J., & Forman, W. R. 1998, ApJ, submitted
Jones, L. R., Scharf, C. A., Perlman, E., Ebeling, H., Wegner, G., & Malkan, M. 1995, in Proc. Röntgenstrahlung from the Universe, ed. H. U. Zimmermann, J. Trümper, & H. Yorke, MPE Report 263 (Garching: MPE), 591
Jones, L. R., Scharf, C. A., Ebeling, H., Perlman, E., Wegner, G., Malkan, M., & Horner, D. 1998, ApJ, 495, 100
Kaiser, N. 1986, MNRAS, 222, 323
Martin, B. R. 1971, Statistics for Physicists (New York: Academic)
McHardy, I. M., et al. 1998, MNRAS, 295, 641
McNamara, B. R., et al. 1998, in preparation
Mohr, J. J., Evrard, A. E., Fabricant, D. G., & Geller, M. J. 1995, ApJ, 447, 8
Nichol, R. C., Holden, B. P., Romer, A. K., Ulmer, M. P., Burke, D. J., & Collins, C. A. 1997, ApJ, 481, 644
Peebles, P. J. E. 1993, Principles of Physical Cosmology (Princeton: Princeton Univ. Press)
Ponman, T. J., Allan, D. J., Jones, L. R., Merrifield, M., McHardy, I. M., Lehto, H. J., & Luppino, G. A. 1994, Nature, 369, 462
Postman, M., Lubin, L. M., Gunn, J. E., Oke, J. B., Hoessel, J. G., Schneider, D. P., & Christensen, J. A. 1996, AJ, 111, 615
Pratt, W. K. 1978, Digital Image Processing (New York: Wiley)
Press, W. H., Teukolsky, S. A., Vetterling, W. T., & Flannery, B. P. 1992, Numerical Recipes (Cambridge: Cambridge Univ. Press)
Rosati, P., Della Ceca, R., Burg, R., Norman, C., & Giacconi, R. 1995, ApJ, 445, L11
Rosati, P., Della Ceca, R., Norman, C., & Giacconi, R. 1998, ApJ, 492, L21
Sandage, A. 1972, ApJ, 173, 485
Scharf, C. A., Jones, L. R., Ebeling, H., Perlman, E., Malkan, M., & Wegner, G. 1997, ApJ, 477, 79
Schmidt, M., et al. 1998, A&A, 329, 495
Soltan, A. M., Hasinger, G., Egger, R., Snowden, S., & Trümper, J. 1996, A&A, 305, 17
Soneira, R. M., & Peebles, P. J. E. 1978, AJ, 83, 845.
Starck, J.-L., & Pierre, M. 1998, A&A, 330, 801
Stocke, J. T., Morris, S. L., Gioia, I. M., Maccacaro, T., Schild, R., Wolter, A., Fleming, T. A., & Henry, J. P. 1991, ApJS, 76, 813
Strag, G., & Nguyen, T. 1995, Wavelets and Filter Banks, (Wellesley: Wellesley-Cambridge Press)
Sunyaev, R. A., & Zeldovich, Ya. B. 1972, Comments Astrophys. Space Phys., 4, 173
Tucker, W. H., Tananbaum, H., & Remillard, R. A. 1995, ApJ, 444, 532
van Haarlem, M. P., Frenk, C. S., & White, S. D. M. 1997, MNRAS, 287, 817
Viana, P. P., & Liddle, A. R. 1996, MNRAS, 281, 323
Vikhlinin, A., & Forman, W. 1995, ApJ, 455, L109
Vikhlinin, A., Forman, W., Jones, C., & Murray, S. 1995a, ApJ, 451, 553
————. 1995b, ApJ, 451, 542
Vikhlinin, A., McNamara, B. R., Forman, W., Jones, C., Quintana, H., & Hornstrup, A. 1998, ApJ, 498, L21
White, S. D. M., Efstathiou, G., & Frenk, C. S. 1993, MNRAS, 262, 1023
White, S. D. M., & Rees, M. J. 1978, MNRAS, 183, 341